Assessing direct CPT-based methods for predicting pile base resistance using coupled DEM-FDM simulations

Chai, Fei; Liu, Bo; Xue, Jianfeng; Duffy, Kevin

DOI
10.1016/j.compgeo.2025.107230

Publication date
2025

Document Version
Final published version

Published in
Computers and Geotechnics

Citation (APA)
Chai, F., Liu, B., Xue, J., & Duffy, K. (2025). Assessing direct CPT-based methods for predicting pile base resistance using coupled DEM-FDM simulations. *Computers and Geotechnics*, *183*, Article 107230. https://doi.org/10.1016/j.compgeo.2025.107230

Computers and Geotechnics 183 (2025) 107230

Contents lists available at ScienceDirect

Computers and Geotechnics

journal homepage: www.elsevier.com/locate/compgeo

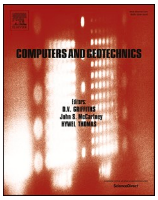

Research Paper

Assessing direct CPT-based methods for predicting pile base resistance using coupled DEM-FDM simulations

Fei Chai [a], Bo Liu [b,*], Jianfeng Xue [a], Kevin Duffy [c]

[a] School of Engineering and Technology, UNSW Canberra, Australia
[b] Department of Civil and Environmental Engineering, The Hong Kong Polytechnic University, Hong Kong, China
[c] Faculty of Civil Engineering and Geosciences, Delft University of Technology, Delft, Netherlands

ARTICLE INFO

Keywords:
Pile base capacity
Direct CPT-based method
DEM-FDM coupling, layered soil
Scale effect

ABSTRACT

This study utilises parallel discrete element method (DEM) simulations of cone penetration tests (CPTs) and pile load tests to investigate the application of direct CPT-based methods for predicting the base capacity of bored piles in layered soils. To reduce boundary effects, a coupled DEM-finite difference method (FDM) model is constructed to simulate pile load tests. The study focuses on the scale effect of pile diameter on the correction factor α_b and the effectiveness of existing q_c averaging methods in layered soils. Two pile diameters and three soil layering conditions, featuring a single silt layer interbedded within sand at varying depths, are considered in the simulations. Results show that both soil layering and pile displacement influence the scale effect. At small settlements (s) up to 0.3 times the pile diameter (D), the scale effect is insignificant, except when a soft layer is directly above the pile tip. At larger settlements, particularly when $s > 0.5D$, piles with smaller diameters show more pronounced reductions in base resistance due to a weak layer closely beneath the tip. Among the four methods evaluated, the BD-18 q_c averaging method produces more consistent α_b values across various soil profiles and pile diameters. Microscopic analysis reveals that soils above the tip contribute less to the pile base resistance at $s/D = 0.1$ than to the cone tip resistance. Additionally, the strength mobilisation levels of soils in most soil layering conditions appear similar at $s/D = 0.1$, supporting the proposal of a constant α_b value in direct CPT-based methods.

1. Introduction

The CPT is increasingly used to establish CPT-based design methods for various types of foundations (Senders and Randolph 2009; Al-Baghdadi et al. 2017; Mayne and Dasenbrock 2018; Bittar et al. 2023) due to its cost-effectiveness, reliability and accessibility in various soil conditions. Utilizing the similarity between CPT instruments and piles, efforts have been devoted to developing direct CPT-based methods for piles (e.g. Bustamante and Gianeselli 1982; Eslami and Fellenius 1997; Clausen et al. 2005; Lehane et al. 2020; Lehane et al., 2022a). In these methods, the pile base resistance (Q_b) is directly correlated with an average cone tip resistance ($q_{c,avg}$) taken over a certain influenced zone surrounding the pile tip through:

$$Q_b = \alpha_b q_{c,avg} \tag{1}$$

where α_b is a correction factor normally less than unity because of the effect of partial mobilisation.

Despite the simplicity of Equation (1), the determination of representative α_b and $q_{c,avg}$ can be challenging, especially when the scale effect and complex soil layering conditions are encountered. For the determination of $q_{c,avg}$, many different cone tip resistance (q_c) averaging methods have been developed and employed, ranging from simple arithmetic or geometric averages, e.g. the LCPC method (Bustamante and Gianeselli 1982) and EF-97 method (Eslami and Fellenius 1997), to methods based on the failure mechanism around the cone or pile, e.g. the De Beer (1971) method and Koppejan method (Van Mierlo and Koppejan 1952), and to more recent averaging procedures involving advanced CPT data manipulation, such as the BD-18 inverse filtering method (Boulanger and Dejong 2018). Specifically, the BD-18 method has recently attracted much attention, including several modifications (Yost et al. 2021; Boorder et al. 2022) and performance examinations (Geyin and Maurer 2021; Bittar et al. 2022). Despite its performance being found generally satisfactory, the efficiency can reduce significantly for highly stratified soil profiles or interlayers with a thickness

---

* Corresponding author.
E-mail addresses: fei.chai@unsw.edu.au (F. Chai), bo-robert.liu@polyu.edu.hk (B. Liu), jianfeng.xue@unsw.edu.au (J. Xue), K.Duffy@tudelft.nl (K. Duffy).

https://doi.org/10.1016/j.compgeo.2025.107230
Received 5 December 2024; Received in revised form 13 February 2025; Accepted 24 March 2025

close to the cone diameter.

For the correction factor α_b, the value recommended in existing direct CPT-based methods varies widely from 0.3 to 1.15, depending on the relative density (Clausen et al. 2005), pile installation method (Bustamante and Gianeselli 1982), and over-consolidation ratio (Van Mierlo and Koppejan 1952; de Kuiter and Beringen 1979), among other factors. Specifically, the recommended α_b value differs across various methods due to the use of different q_c averaging methods. For instance, the α_b value recommended for bored piles is 0.35 in the Dutch method which employs the Koppejan averaging method, while the LCPC method suggests an α_b value ranging from 0.3 to 0.4, depending on the magnitude of $q_{c,avg}$. This creates inconsistencies in uniform soils where all averaging methods result in the same $q_{c,avg}$.

Additionally, there is a continuing debate regarding whether α_b is influenced by pile diameter, a phenomenon commonly referred to as the 'scale effect'. Chow (1997) found a logarithmic relationship between α_b and pile diameter when using the base capacity at the settlement of 0.1D and the LCPC averaging method. Additionally, Jardine et al. (2005) suggested that α_b reduces as the pile diameter increases, but an opposite trend was observed in small-scale centrifuge tests (Klotz and Coop 2001). Nonetheless, Lehane et al. (2007) recommended a constant α_b for all pile diameters. White and Bolton (2005) pointed out that the scale effect exhibited by the α_b values derived from field pile load tests arises from effects of partial embedment, residual stresses and partial mobilisation, and eliminating these effects leads to α_b values independent of pile diameter. Specifically, the authors accounted for the effect of partial embedment of pile tip into a bearing stratum by employing a different q_c averaging approach. This suggests whether an 'apparent' scale effect on α_b exists or not depends on the q_c averaging approach used.

Understanding the penetration mechanism and stress distribution induced by CPT installation or loading a pile is essential for addressing the limitations of existing q_c averaging approaches, as well as understanding the dependency of α_b on the factors mentioned above. In existing studies, the employment of image-processing techniques (White and Bolton 2004; Arshad et al. 2014; Ganju et al. 2021) and high-quality stress transducers (Lehane 1993; Jardine et al. 2013a, b; Yang et al. 2014) has enabled detailed analysis of the penetration mechanism and extreme stress changes occurring within the vicinity of penetrometers or pile tips, respectively. However, these have rarely been conducted in layered soils to reveal the effect of soil layering on the induced displacements and stresses. This deficiency limits our understanding of the mechanistic origin of α_b's sensitivity to various factors, particularly the scale effect, thereby impeding the further refinement of direct CPT-based design methods for piles.

Most existing studies have primarily focused on the application of direct CPT-based methods to displacement piles, while the investigation on bored piles remains relatively limited. Compared to bored piles, the installation of displacement piles results in increased stresses and densities in the surrounding soils (Yang et al. 2014; Duan et al. 2018; Kabeta 2022), akin to the conditions created around a cone penetrometer. This similarity facilitates the use of CPT-based methods for displacement piles. However, the installation of bored piles is typically considered to have minimal influence on surrounding soils, which is why they are usually modelled as "wished-in-place" (Duan et al. 2018; Su et al. 2022). This difference between displacement and non-displacement piles has been addressed by simply employing a reduced α_b value for bored piles in existing CPT-based methods (Van Mierlo and Koppejan 1952; De Beer 1971; Bustamante and Gianeselli 1982). An improved understanding of the application of CPT-based methods for bored piles is clearly needed.

To address these gaps, this study employs DEM to conduct parallel simulations of CPT penetration and pile load tests in layered soil profiles. Notably, existing DEM simulations have rarely investigated CPT or pile load tests in layered soils. To reduce boundary effects while maintaining the particle number manageable, a coupled DEM-FDM model is constructed to simulate the pile load tests, allowing soils adjacent to the pile to be simulated using particles in DEM. The surrounding soils, which primarily serve as a deformable boundary condition, were modelled with FDM meshes that require fewer computational resources. Two pile diameters (D) are considered: 0.1 and 0.15 m. The soil systems under investigation feature a single weak silt layer (0.15 m thick) interbedded in sand at various depths near the pile base. The simulated q_c profile and load-settlement response of piles are utilised to study the scale effect on α_b, the performance of different q_c averaging approaches in layered soils, and the effect of soil layering on the force chain development and stress distribution around the piles.

2. DEM simulations

2.1. Model set-up

In this study, DEM simulations of CPTs were conducted using PFC3D 7.0 software, while the pile load tests were simulated using coupled DEM-FDM models based on the coupling algorithm integrated in PFC3D 7.0 and FLAC3D 7.0.

Because the major emphasis of this study is placed on pile responses, for simplicity, the DEM model for conducting CPT drilling was constructed following the earlier work by Khosravi et al. (2020). The DEM modelling of CPT tests in calibration chamber was performed using a cone penetrometer with a diameter (D_c) of 0.044 m in a soil column contained within a cylindrical chamber, as shown in Fig. 1(a). The diameter and height of the chamber are 0.7 m and 1 m, respectively, achieving a chamber-to-cone diameter ratio of 15.6, comparable to those used in existing studies (Arroyo et al. 2011; McDowell et al. 2012; Butlanska et al. 2014). In the calibration chamber, a servo-control mechanism was employed to apply constant lateral and vertical stresses to the soil column by controlling the displacement of the chamber walls. In the current simulations, a radial stress of 50 kPa and a vertical stress of 100 kPa were considered, resulting in a K_0 value of 0.5 for the considered material, where K_0 is the lateral earth pressure coefficient at rest. Nominally uniform stresses throughout the chamber were achieved by ignoring gravity in the CPT simulations. The dimensions of the chamber and cone, along with the boundary conditions, are summarised in Table 1.

For the pile load tests, small pile diameters (D) of 0.1 and 0.15 m were considered because achieving realistic D/D_c ratios for typical field piles would require over 50 million particles, which exceeds the available computational capabilities. Therefore, the influence range of these piles is smaller than that of field piles, leading to a more pronounced effect of an adjacent weak layer. This suggests that directly applying the simulated Q_b or α_b in layered soil conditions to practical scenarios is not feasible. Additionally, it is highly computationally intensive to simulate a complete pile in DEM since a large particle number is required to achieve an acceptable pile-to-particle diameter ratio. Considering that the pile tip resistance is concerned in this study, the pile load tests were also simulated in a calibration chamber, a simplification previously employed by many researchers (e.g. Lee and Salgado 2000; Bagbag et al. 2019). The coupled numerical model for the pile load tests consists of a cuboid DEM subdomain, measuring 2.5D in width and 12D in height, encased within an FDM subdomain with dimensions exceeding 30D in width and length, as shown in Fig. 1(b). Pile penetration was conducted within the DEM subdomain, where large deformations can be accommodated, while the FDM subdomain served as a flexible boundary to minimise boundary effects.

Communication between the two subdomains was achieved by constructing virtual boundary walls in the DEM subdomain, which correspond in exact geometries and positions to the interfacial FDM mesh faces. For the deformation compliance between the two subdomains, displacements of the mesh nodes at the subdomain interface were sent to the DEM code for updating the position of virtual wall elements, which serve as moveable boundaries for the DEM particle assembly. Meanwhile, the force balance and stress continuity at the subdomain interface were achieved by converting the interaction forces

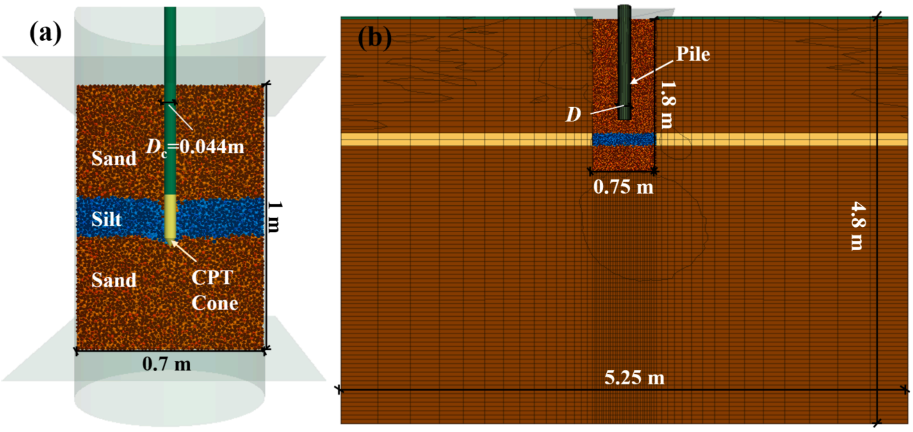

Fig. 1. Model set-up for a) the DEM model for cone penetration test, and b) the coupled DEM-FDM model for pile load test in multilayered soil systems.

Table 1
Model geometry parameters for the CPT and pile loading tests.

Model	CPT	Pile loading test	
	DEM	DEM subdomain	FDM subdomain
N_e*	152,604	393,519	204,176
Model geometry	Cylinder	Box	Box
D_c (m)	0.044	–	
D (m)	–	0.15 ($3D_c$) or 0.1 ($2D_c$)	
Model diameter (m)	0.7	2.5D	40D
Model height (m)	1.0	12D	36D

Note: * N_e is the number of elements in the corresponding numerical model, which is particle number in DEM and zone number in FDM.

between the soil particles and the virtual wall elements into nodal forces acting on the nodes of the corresponding FDM meshes based on barycentric interpolation. Such a modelling strategy has previously been employed in many studies (Indraratna et al. 2015; Jia et al. 2018; Jia et al. 2021; Yin 2022) to avoid using an excessive number of particles while minimising boundary effects. The top surface of the model was subjected to a constant pressure of 80 kPa, resulting in vertical stresses at the pile tip of approximately 100 kPa, as gravity was considered in this case. Other boundaries of the FDM subdomain were simply fixed in position due to their large distance from the DEM subdomain. Details of the coupled DEM-FDM model are also summarised in Table 1.

2.2. Materials and parameters

The same soil layering and materials were considered in the simulations of the calibration chamber CPTs and the pile load tests. As shown in Fig. 1, the layered soil sample consists of a silt layer interbedded within uniform sand layers, with the silt representing the weaker interlayer. In this study, all soils were represented by assemblies of spherical particles, with the interactions between the particles simulated using the linear rolling resistance contact model provided in the software package (Itasca Consulting Group 2021). In this contact model, a rolling resistance moment is introduced at the contact point to account for increased resistance to rolling of non-spherical particles (Iwashita and Oda 2000; Jiang et al. 2005; Wang et al. 2024).

The sand layers in the layered systems were generated to mimic Ottawa 20–30 sand. The grain size distribution of this sand has been reported by Su et al. (2019). To maintain the computational cost affordable, the particle sizes of Ottawa 20–30 sand have been scaled up by a factor of 20, resulting in virtual sand particle sizes between 12.4 and 16.4 mm, with a median (d_{50}) of 14.3 mm. Note that the ratio between the penetrometer diameter and the median grain size (D_c/d_{50}) is 3.07, which is greater than the threshold value of 2.7 established by Arroyo et al. (2011), suggesting that the particle size effect can be expected to be small. The weak silt layer interbedded in the sand layers was generated to mimic the sandy material tested by Pietruszczak et al. (2003). As will be shown later, this material behaves similarly to silt in terms of SBTn classification. Because the gradation information is not reported, the same grain size distribution of the virtual sand particles was used to simulate the silt.

The micromechanical parameters of the sand and silt were calibrated against the triaxial test responses of Ottawa sand (Alshibli et al. 2003; Su et al. 2019) and of the silt (Pietruszczak et al. 2003), respectively. The calibrated micromechanical parameters are summarised in Table 2. The triaxial shear responses simulated with these parameters are compared with the measured responses in Fig. 2, where good agreement is found for Ottawa sand. For the silt, the moderate deviations between the simulated and measured triaxial response after an axial strain of about 3 % can be considered acceptable considering the limited data available for this material.

The constitutive model employed for the FDM subdomain was the -Mohr-Coulomb model, and the parameters were determined from DEM triaxial simulations conducted on the corresponding granular assemblies. The triaxial simulations indicate that the sand has a secant Young's modulus of 70 MPa at an axial strain increment of about 0.1 % and a peak friction angle of 41°. Note that the secant modulus at an axial strain increment of 0.1 % was selected because this is the strain level experienced by soils in the vicinity of typically geotechnical structures (Burland 1989; Atkinson 2000; Lehane and Cosgrove 2000). The macroscopic mechanical properties determined from the triaxial simulations were assigned to the sand layers in the FDM model. For the silt,

Table 2
Material parameters of sand and silt in the DEM and FDM models.

Model	Soil Parameters	Sand	Silt
DEM (PFC)	Contact model	Linear rolling resistance	
	Particle size (d_{50}): mm	0.0143	0.0143
	Particle density (ρ_s): kg/m^3	2650	2650
	Initial porosity	0.367	0.375
	Porosity after consolidation	0.38	0.389
	Contact normal stiffness (k_n): MN/m	5.0	0.4
	Contact tangential stiffness (k_s): MN/m	2.5	2.0
	Inter-particle friction coefficient	0.35	0.28
	Damp ratio	0.7	0.7
	Rolling friction coefficient	0.4	0.38
FDM (FLAC)	Constitute model	Mohr-Coulomb	
	Density (ρ): kg/m^3	1650	1640
	Elastic bulk modulus (K): MPa	150	47
	Young's modulus (E): MPa	70	25
	Poisson's ratio (ν)	0.296	0.263
	Friction angle (ϕ): degree	40	31

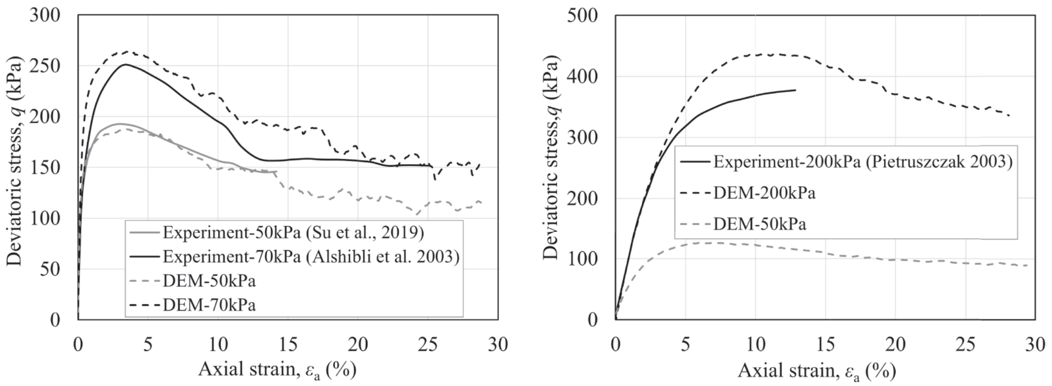

(a) Ottawa sand (b) the silt

Fig. 2. Comparison between the simulated and experimental triaxial shear responses of the sand and the silt.

the triaxial simulations predict a secant Young's modulus of 9 MPa and a friction angle of 31°. However, to minimise significant compression of the silt layers during the stress installation phase (discussed later), the modulus of the silt layer in the FDM model was adjusted to 25 MPa. Table 2 summarises the material parameters for both the DEM and FDM models. The interaction between the particles and the chamber walls or the penetrometer/pile was simulated using the linear elastic model, and the stiffness parameters were assigned values twice those between corresponding particles to simulate rigid chamber walls or penetrometers (Jia et al. 2021). A small frictional coefficient of 0.1 was adopted between the virtual soil particles and the chamber walls to improve the stability of the servo-control mechanism following Khosravi et al. (2020). A frictional coefficient of 0.2, experimentally measured between a penetrometer sleeve and Ottawa sand (Martinez and Frost 2016), was assigned to both the penetrometer cone and the pile.

Fig. 3 shows the simulated CPT q_c profiles in the homogeneous sand, the silt, and the layered soil system with a 0.15 m thick silt layer sandwiched between layers of sand. The average q_c values for the homogeneous sand and the silt are 7.82 MPa (Fig. 3(a)) and 1.98 MPa (Fig. 3(b)), respectively. The Soil Behaviour Type index (I_{sbtn}) (Robertson 2009) successfully identified the soils as sand and silt based on the simulation results. Additionally, Sadrekarimi (2016) conducted a series of laboratory calibration chamber CPTs in loose to medium-dense Ottawa 20–30 sands and derived an empirical relationship for predicting the q_c value, as given by Equation (2). The relative density of the DEM assembly was estimated to be 58 %, based on the maximum and minimum void ratios of 0.72 and 0.48, respectively. These threshold void ratios were determined by assigning frictional coefficients of 5 and 0 to the particles during sample preparation, following Sazzad et al. (2014). Fig. 4 shows that the simulated q_c closely aligns with Equation (2), highlighting the model's credibility.

$$\frac{q_c}{(\sigma_v)^{0.612}} = 0.119\exp\left(\frac{2.55D_r}{100}\right) \tag{2}$$

In Fig. 3(c), the q_c profile for the layered sample reveals a transition zone due to the presence of the thin, weak layer. The q_c value gradually decreases from approximately 7.5 MPa in the top sand layer to about 2.9 MPa in the middle of the silt layer, before increasing again to 7.5 MPa in the bottom sand layer. This transition effect has been observed in many calibration chamber and centrifuge CPTs (de Lange et al. 2018; Bittar et al. 2022; Khosravi et al. 2022). Due to particle interactions near the interface, only soils in the middle of the interlayer can be identified as silt, consistent with existing laboratory tests.

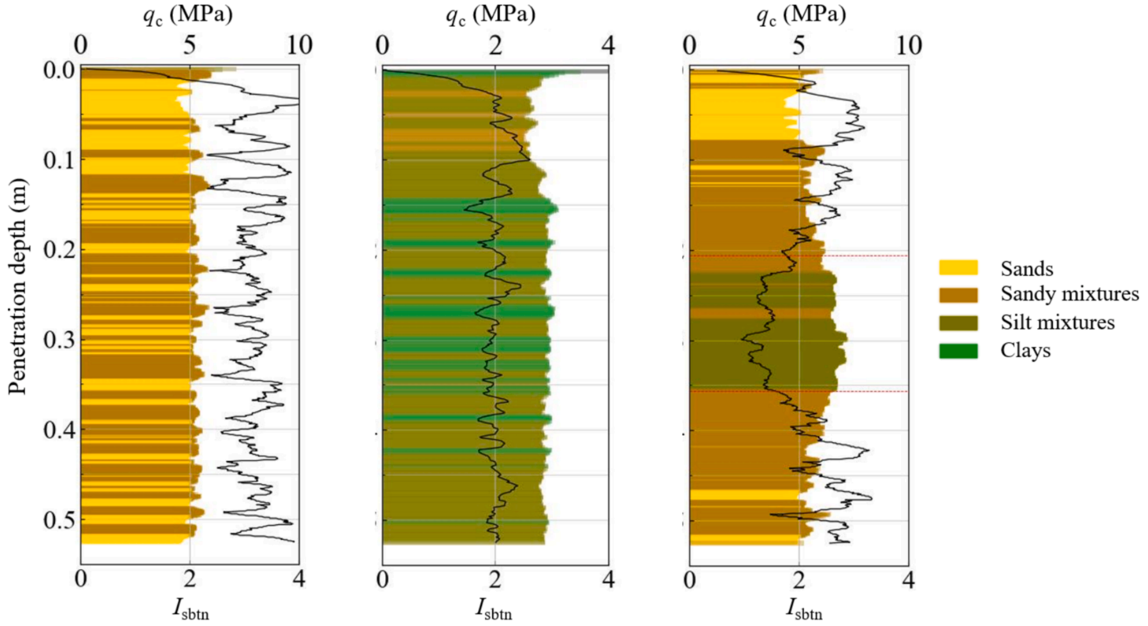

(a) Homogenous sand (b) Homogenous silt (c) 0.15m silt sandwiched between sand

Fig. 3. q_c profiles obtained from the CPT simulations and the corresponding SBTn classification.

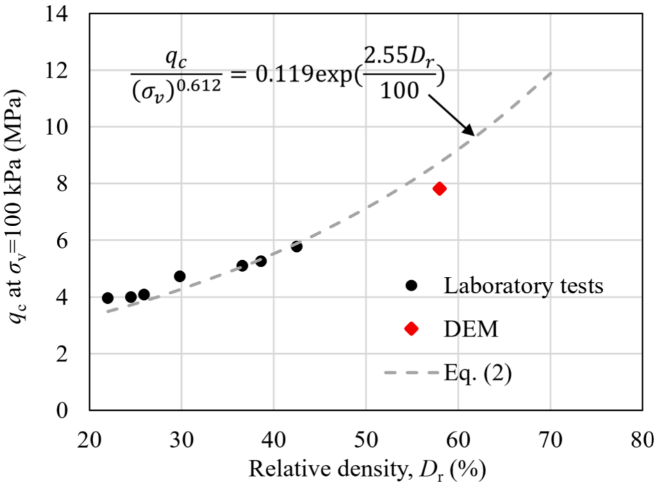

Fig. 4. Comparison between the simulated and measured q_c values for Ottawa 20–30 sand with different relative densities under $\sigma_v = 100$ kPa; experimental results from Sadrekarimi (2016).

2.3. Simulation program and procedures

The same sample preparation method and parameters were used to prepare equivalent DEM assemblies in the CPT simulations and the pile load tests. The homogeneous and layered soil samples were generated using the radius expansion method. Particles representing Ottawa sand and the silt were generated simultaneously in their respective regions but were assigned different micromechanical properties. After that, the servo-control mechanism of the boundary walls was activated to install the required K_0 stress condition. The frictional coefficients between the particles were the same as those used in the triaxial simulations. This sample preparation method has been shown to produce fairly uniform porosities across each soil layer, and the porosity and fabric in the DEM sample (for CPTs) and the DEM subdomain (for pile load tests) are also similar. The porosities of the sand and the silt layers after applying the K_0 stress condition were 0.38 and 0.389, respectively. After sample preparation, the frictional coefficients in Table 2 were assigned to the corresponding particles.

For CPT simulations, after the calibration chamber reached equilibrium under the imposed K_0 stress condition, the penetrometer was pre-embedded 0.2 m deep ($4.5D_c$) into the sample to avoid the shallow penetration effect and facilitate the attainment of steady-state q_c (Lehane et al. 2022b). The model was cycled again to equilibrium after the soil particles overlapping the penetrometer were deleted. After that, penetration was conducted at a rate of 0.05 m/s, which corresponds to an inertial number of about 1.0×10^{-3}, meeting the requirement of a quasi-static condition (Da Cruz et al. 2005; Lopera Perez et al. 2016). Note that the inertial number is defined as $I = \dot{\varepsilon} d_{50}\sqrt{\rho_s/p'}$ where d_{50} is the mean particle size, ρ_s the particle density, p' the effective confining pressure, and $\dot{\varepsilon}$ the shear strain rate estimated assuming that all compression occurs within $3D_c$ depth below the cone tip (Yang 2006; Cerfontaine et al. 2021). The penetration continued until the cone travelled for 0.55 m ($12.5D_c$) to a terminal depth of 0.75 m, leaving a clearance of 0.25 m ($5.6D_c$) to the chamber bottom. No clear bottom boundary effect can be observed in the q_c profiles recorded until this depth, as shown in Fig. 3(a) and 3(b).

For the pile load tests, an FDM model for the whole sample was constructed and cycled to equilibrium before coupling with the DEM subdomain. After both subdomains had reached initial equilibrium, the FDM zones overlapping with the DEM subdomain were deleted and then the coupling between the two subdomains was initiated. After the coupled model was cycled to equilibrium, the pile was generated using rigid wall elements, with the tip at $8D$ depth below the surface. Note that the critical depth beyond which the base resistance remains constant for bored piles in sand is calculated to be about $8.2D$ for the current model, using the empirical relation proposed by Poulos and Davis (1980). This indicates that the simulated pile tip resistance will not be subjected to any pronounced shallow penetration effect. After generating the pile, particles overlapping with the pile were deleted, and the model was cycled to equilibrium again before load testing. The above installation procedures were designed to simulate bored piles. As will be demonstrated later, this installation method resulted in only slight reductions in stresses within the surrounding soil.

In this study, three simulations of CPT penetration and eight pile load tests were performed. Two CPT simulations were conducted in the homogeneous sand and the homogeneous silt samples, and the remaining one was conducted to provide CPT soundings in a layered soil with one 0.15 m-thick silt layer sandwiched between sand layers. Similarly, two pile load test simulations were conducted in the homogeneous sand and the silt samples, which are labelled as Tests 1 and 2 in Table 3. To investigate the effect of pile diameter on the tip resistance correction factor α_b, piles of two different diameters (0.1 and 0.15 m; about $2D_c$ and $3D_c$) were simulated in the layered soil samples. For each pile diameter, three scenarios were considered based on the initial distance (L_w) of the pile tip to the top surface of the weak layer: L_w = -0.15 m (Tests 3 and 6), $L_w = 0$ (Tests 4 and 7) and $L_w = 0.15$ m (Tests 5 and 8). These scenarios are demonstrated in Fig. 5. Positive values of L_w indicate that the weak layer is below the pile tip, and vice versa. In practice, piles are typically designed to end on a strong bearing layer, maintaining a sufficient distance from the nearest weak layer(s). Thus, the scenario $L_w = 0$ demonstrated in Fig. 5(b) is unrealistic, while in the other two cases ($L_w = \pm 0.15$; Fig. 5(a) and 5(c)), the effect of the weak layer is exaggerated, as the distance to the weak layer is smaller than what is typically observed in field tests (e.g. Lehane 1993; Chow 1997; Gavin et al. 2015). However, these cases are designed to better examine the capability of various q_c averaging methods in extreme soil conditions. The loading scheme employed in the pile load test simulations was optimised with respect to computation efficiency, as will be discussed later.

3. Macroscopic results and analysis

3.1. Effect of loading methods

The potential effects of loading methods on the pile base resistance are investigated by performing two loading procedures: staged load-controlled (LC) method to a total settlement of $1D$ and displacement-controlled (DC) penetration to $0.3D$ settlement. In the DC simulations, piles were loaded vertically at a constant rate of 0.05 m/s, and loading was stopped after reaching a pile settlement of $0.3D$ due to the long duration required. In the staged LC simulations, the pile movement was controlled by a servo-control mechanism to attain a specified pile base resistance at each stage while maintaining the pile vertical. The target pile base stresses were sequentially increased to the following values: 0.7, 1.4, 2.2, 3.0, 5.0, and 7.0 MPa, with additional increments as required. The load increased to the next value once the settlement stabilised (indicated by an average force unbalanced ratio falling below 1×10^{-4}).

Table 3
Summary of the pile load test simulations.

Test. No	Pile diameters	Model description
1	0.15 m (~$3D_c$)	Homogeneous sand
2		Homogeneous silt
3	0.15 m (~$3D_c$)	L_w = -0.15 *m*
4		$L_w = 0$
5		L_w = 0.15 *m*
6	0.1 m (~$2D_c$)	L_w = -0.15 *m*
7		$L_w = 0$
8		L_w = 0.15 *m*

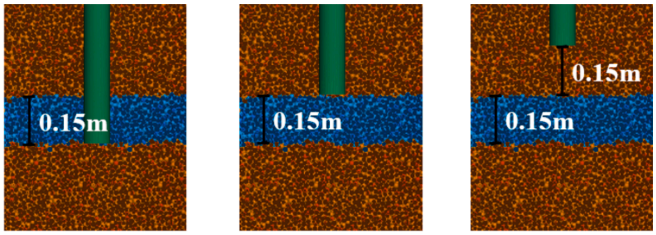

(a) $L_w = -0.15$ m (b) $L_w = 0$ (c) $L_w = 0.15$ m

Fig. 5. Demonstration of various arrangements of pile relative to the weak layer.

Fig. 6 compares the load–displacement curves obtained for Tests 1 and 4 using the staged LC and DC methods. The curves obtained with the DC method are shown as bold solid lines, while those for the staged LC method are marked with symbols. It is important to note that the settlement plunges during each load stage do not represent the 'creep' behaviour typically observed in field tests (Fellenius et al. 2004; Olson and Shantz 2004; Han et al. 2017). Instead, this simply reflects the process to attain stabilisation upon a sudden increase in the target base resistance. The pile moved quickly initially due to the large difference between the current resistance and the target value. As the difference between these values decreased, the pile movement slowed down. Once the pile capacity reached the target value and the soil system stabilised, the settlement reached a value representative of the quasi-static response of the pile at the target resistance. Thus, the data points at the end of each loading stage from the LC method are connected to form a 'fitted ultimate' curve, represented by broken lines in the figure. The comparison demonstrates that the 'fitted ultimate' curve obtained with the staged LC method (broken lines) closely matches the DC method curve (bold solid lines up to 0.3*D* settlement), indicating that the loading scheme does not significantly affect the pile response in the numerical models used in this study.

As also shown in the figure, for Test 4 with a silt layer directly beneath the pile base, a punching failure can be observed at the loading level of about 5 MPa, where very large settlement occurred during this stage, and increasing the target resistance to 6 MPa resulted in a temporary increase of pile resistance followed by a sudden drop back to values of around 5 MPa. Thus, the ultimate pile base capacity for the model with a 0.15 m-thick silt layer just below the pile base can be determined to be 5 MPa.

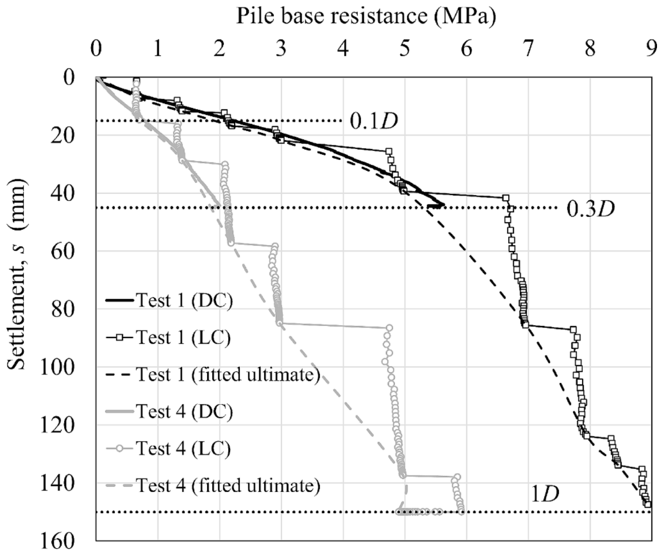

Fig. 6. Load–settlement responses of piles obtained with different loading methods; DC and LC stand for the displacement-controlled and the load-controlled method, respectively.

3.2. Effect of failure criteria

Fig. 7 displays the load–settlement responses of the piles tested under various soil layering and pile diameter conditions. The settlements (*s*) are normalised by the pile diameter (*D*). Fig. 7(a) shows the behaviour of the piles up to the settlement of 0.3*D* obtained with the DC method for studying the pile responses in the initial loading range. Fig. 7(b) shows the behaviours of the piles up to the settlement of 1*D* obtained with the LC method for studying the ultimate bearing capacity of the piles. In the figures, the response of piles in the homogeneous soil samples is indicated with red lines, with those of the large-diameter ($D = 0.15$ m) and the small-diameter ($D = 0.1$ m) piles indicated with solid and broken lines, respectively.

Fig. 7(a) shows that for the load-settlement response up to 0.1*D* settlement, when the weak layer is below the pile base, the bearing capacities of piles with greater diameters (Tests 4 and 5) are only slightly greater than those of the smaller piles (Tests 7 and 8), indicating a negligible scale effect. However, when the weak layer is located above the pile tip (Tests 3 and 6), the base resistance of the larger pile (Test 3) is comparable to that in the uniform sand and considerably greater than that of the smaller pile (Test 6). The slightly higher mobilised bearing stress in Test 3 compared to Test 1 (homogeneous sand) may arise from slight variations in the void ratios between different samples.

For the load–settlement responses at $s/D > 0.3$, the presence of a weak silt layer below the pile base (Tests 4 and 5 for $D = 0.15$ m and Tests 7 and 8 for $D = 0.1$ m) is seen to reduce the pile base resistance significantly, and the load–settlement responses are closer to that that in the homogeneous silt sample (Test 2). When the weak silt layer is situated above the pile base (Tests 3 and 6), the silt layer only has a marginal effect on the load–settlement responses at $s/D > 0.3$. Comparing Fig. 7 (b) to Fig. 7(a), it is found that the contribution of the underlying weak layer is greater at larger s/D values, suggesting that the relative importance of different soil layers is also affected by s/D. Additionally, the punching failure occurred for piles with a silt layer below the pile base (Fig. 7(b)). In Tests 4 and 7, with the silt layer directly below the pile base, the load–settlement response of the large pile (Test 4) deviates from that of the small pile (Test 7). This is due to the different influence depths of the piles, which affects the contribution of the underlying silt layer.

Overall, it can be concluded that in the initial loading stages (up to 0.3*D* settlement), the scale effect on pile base resistance is insignificant, unless a soft layer is directly above the pile tip. However, in the later loading stages, especially when $s > 0.5D$, pile diameter influences the pile base responses if a weak layer is located closely below the tip. For piles with the same distance to the silt layer but different diameters, the base resistance of the pile with a larger diameter appears to be less weakened by the silt layer, as indicated by the greater capacity obtained from Test 4 ($D = 0.15$ m) over that from Test 7 ($D = 0.1$ m), where in both cases the silt layer is located right below the pile base. This effect becomes less significant when the silt layer is 0.15 m deeper (Tests 5 and 8).

The pile base resistances in homogeneous soil samples obtained from Tests 1 and 2 at the settlement of 0.1*D* ($Q_{b\_0.1D}$) and 1*D* (Q_{b_1D}) are compared in Fig. 8. The former corresponds to the typical bearing capacity used in design, recommended in many standards (ISSMFE 1985; BSI 2015), while the latter can be taken as the ultimate bearing capacity (White and Bolton 2005). The figure shows that the simulated Q_{b_1D} closely approximates the q_c values, which is consistent with the findings of White and Bolton (2005) and Gavin and Lehane (2007). The comparable Q_{b_1D} and q_c values demonstrate that the samples used in the CPT simulations and the pile load tests exhibit equivalent mechanical behaviour. The ratio between $Q_{b\_0.1D}$ and Q_{b_1D} for piles in the homogeneous sand and silt is 0.28 and 0.17 respectively in this study. The

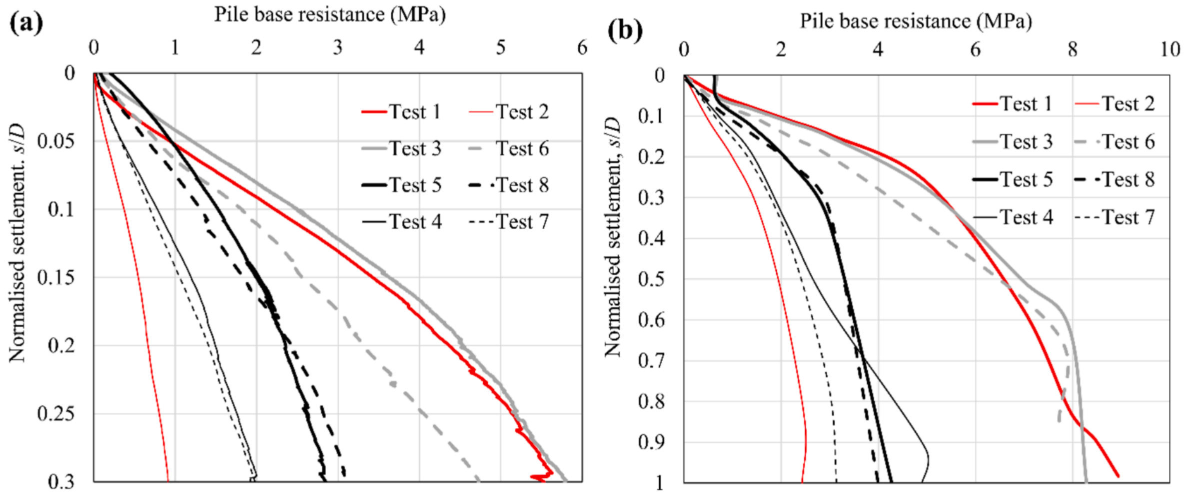

Fig. 7. Load-settlement curves of the piles up to a settlement of (a) 0.3D using the displacement-controlled loading and (b) 1D using the load-controlled loading.

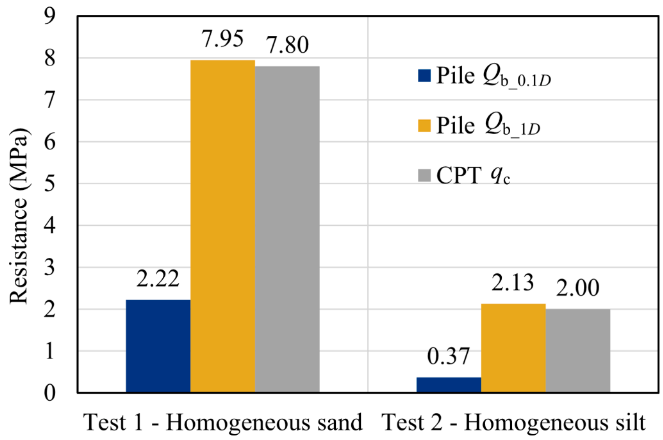

Fig. 8. Comparison of $Q_{b\backslash\_0.1D}$, $Q_{b\backslash\_1D}$ and q_c in the homogeneous samples.

ratio for the sand sample falls between the α_b values of 0.2 recommended in the European design methods (e.g. see De Cock et al. 2003) and 0.35 recommended in the Dutch Standard (NEN9997-1, 2016) for full replacement-bored piles, while the ratio for the silt is lower than the recommended values.

Fig. 9 summarises the simulated $Q_{b\_0.1D}$ and Q_{b_1D} for piles of different diameters in the layered samples in comparison to the corresponding q_c values recorded at the pile tip level. Fig. 9(a) shows that when the weak layer is below the pile tip ($L_w = 0$ and 0.15 m), the pile dimension has a small influence on $Q_{b\_0.1D}$. The difference in the values of $Q_{b\_0.1D}$ between the two piles with different diameters is less than 11 %. However, when the weak layer is located above the pile tip (L_w = -0.15 m), a large difference of 25 % in $Q_{b\_0.1D}$ was observed between the two piles. In contrast, an opposite trend is observed for Q_{b_1D} at larger strength mobilisations. In Fig. 9(b), the presence of a weak layer below the pile tip ($L_w = 0$ and 0.15 m) leads to a considerable variation in the base resistance across different pile sizes (37 % for $L_w = 0$ and 17 % for $L_w = 0.15$ m), while only a smaller difference of 7 % is observed for the cases with the pile tip at the bottom of the weak layer (L_w = -0.15 m). Overall, the scale effect is influenced by both the soil layering and the level of pile displacement at which the effect is examined.

3.3. *Performance of q_c averaging approaches*

In Fig. 9(b), the q_c values recorded at the pile base level in layered samples can differ significantly from the ultimate bearing capacity (Q_{b_1D}) of piles, indicating that the CPT soundings recorded in layered soils should be properly averaged before being used to predict the pile base resistance. The performance of four existing averaging methods, i.e. the Koppejan, the LCPC, the BD-18, and the De Beer methods, to provide representative $q_{c,avg}$ values in layered soils was examined based on the DEM simulation results.

3.3.1. *CPT profile*

The CPT profiles obtained from the DEM simulations (Fig. 3) are only

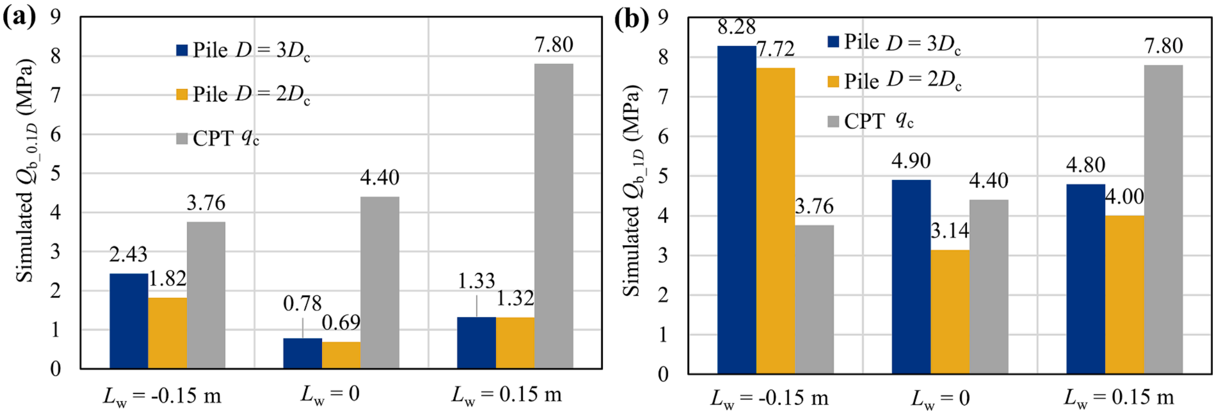

Fig. 9. Comparison of (a) $Q_{b\_0.1D}$, (b) Q_{b_1D} with q_c for different pile diameters in the layered soil samples.

0.55 m in length, which is insufficient for calculating $q_{c,avg}$ in some averaging methods. Therefore, proper extrapolation should be allowed for constructing an equivalent in-situ CPT profile. Considering that the vertical stress of 100 kPa is approximately equivalent to a 6.5 m overlying soil layer, an 8 m length CPT profile was generated with a 0.15 m thin silt layer between 6.7 and 6.85 m.

A CPT data processing procedure has been developed to generate an 8 m CPT profile as demonstrated in Fig. 10. In Step 1, an 8 m CPT profile in a homogenous sand sample was generated as shown in Fig. 10(a) based on the statistical features (a mean value of 7.8 MPa and a standard deviation of 1.1 MPa) of the simulated q_c profile in the homogeneous sand sample presented in Fig. 3(a). In Step 2, the CPT profile in a 0.5 m-thick layer containing the thin weak layer was generated based on the simulated CPT profile obtained in the layered soil sample. The 0.3 m-thick central segment (coloured in red in Fig. 10(b)) was directly replaced with the corresponding CPT soundings recorded in the simulation, while the remaining top and the bottom segments (coloured in green in Fig. 10(b)) were generated based on a linear regression to achieve a smooth transition to the mean q_c value in the homogeneous sand sample. In Step 3, the segment between 6.5 and 7.0 m in the 8 m profile (in light grey in Fig. 10(a)) was replaced with the 0.5 m profile generated in Step 2 to construct an 8 m CPT profile with a 0.15 m thick silt layer at a depth of 6.7 m, as shown in Fig. 10(c). The q_c profile generated with the above procedures corresponds to a sensing distance of $4D_c$ and a development distance of $3D_c$. Additionally, the generated CPT profile was further processed to achieve a consistent 0.2 m spacing for all cases, ensuring that data quantity and spacing do not introduce any bias on different averaging methods.

3.3.2. $q_{c,avg}$ from four averaging methods

Different methods have been developed in the literature to obtain the $q_{c,avg}$ values. The popular ones include the Koppejan method (Van Mierlo and Koppejan 1952), the LCPC method (Bustamante and Gianeselli 1982), the classic semi-empirical De Beer (1971) method, and the BD-18 method (Boulanger and Dejong 2018).

In the Koppejan method, $q_{c,avg}$ is a sequential pairwise average of three values, q_{cI}, q_{cII} and q_{cIII}, calculated using Equation (3).

$$q_{c,avg} = [(q_{cI} + q_{cII})/2 + q_{cIII}]/2 \tag{3}$$

where q_{cI} is the arithmetic average q_c values over the depth of $0.7D$ to $4D$ below the pile tip; q_{cII} and q_{cIII} represent the arithmetic averages of q_c following the minimum path rule (Fig. 11(a)) over $0.7D$ to $4D$ below the pile tip and 0 to $8D$ above the pile tip, respectively. Detailed explanations can be found in Xu (2007).

The LCPC method applies an influence zone of $1.5D$ above and below the pile tip. It starts by smoothing the q_c profile, removing values below 0.7 and above 1.3 times the average value, and subsequently calculating the arithmetic average of the remaining values, as illustrated in Fig. 11 (b).

Besides these empirical averaging methods, the classic semi-empirical De Beer method is also widely used to predict the ultimate pile base resistance. This method particularly emphasises the scale effect and the transition of q_c values through different soil layers. This method acknowledges the fact that when the cone/pile transfers from the weaker layer to the stronger layer, a larger pile needs a greater critical depth to reach the full resistance of the stronger layer (Xu and Lehane 2008; Khosravi et al. 2022). In other words, the transmission of resistance from a weaker to a stronger layer will be slower for a pile compared to a CPT.

In the BD-18 method, both q_c and $q_{c,avg}$ are considered the convolved 'true' q_c, denoted as $q_{c:true}$, with a diameter-dependent moving filter. In other words, q_c can be taken as the sum of $w \bullet q_{c:true}$ along the depth of the CPT profile, where w is a weighting factor influenced by two parameters w_1 and w_2, which account for the relative distance between the soil and the pile tip, and the relative stiffness between the soil layers, respectively.

The CPT profile generated above for a layered sample was analysed for comparison of $q_{c,avg}$ values obtained with the four averaging methods. Fig. 11 provides the visual representations of the procedures used in these methods. Table 4 presents the $q_{c,avg}$ values obtained with these methods under various soil conditions and pile diameters. Generally, under the same soil condition, the Koppejan method yields the lowest $q_{c,avg}$, followed by the De Beer method. The LCPC and the BD-18 methods produce higher $q_{c,avg}$ values. Additionally, the coefficients of variation (CoV) in the $q_{c,avg}$ values obtained from the four methods are below 10 % in the homogeneous samples but around 18 % to 28 % in layered samples, suggesting that the disparity between the methods is more pronounced in layered samples.

Table 4 also shows that the sensitivity of the obtained $q_{c,avg}$ values to the weak layer position varies for different averaging methods. The Koppejan and the De Beer methods result in low percentage differences (PDs) between the $q_{c,avg}$ values obtained for different-sized piles (0 % for

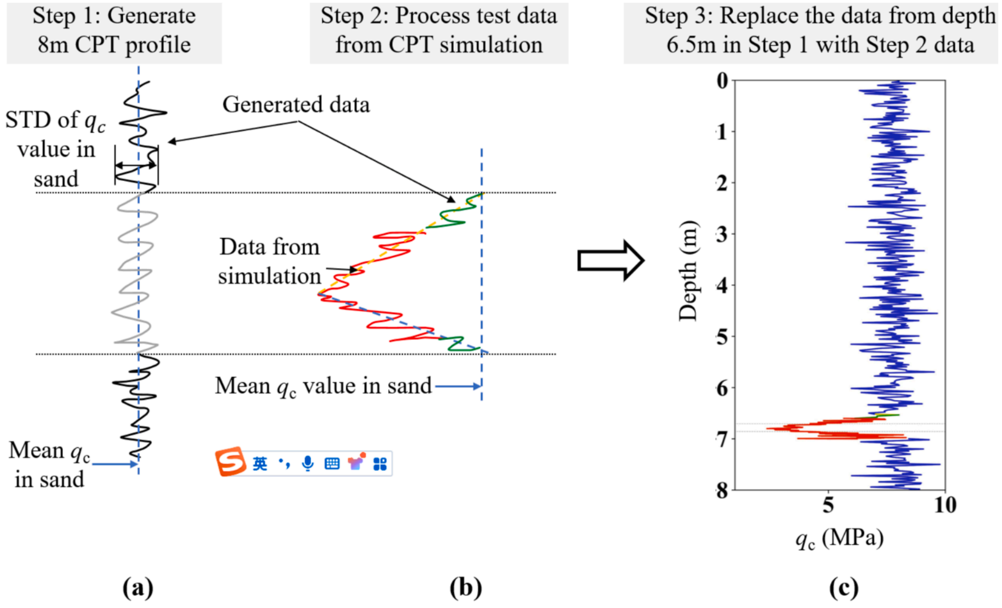

Fig. 10. Illustration of the CPT data process procedures based on the simulated CPT profiles in the interlayered soil sample.

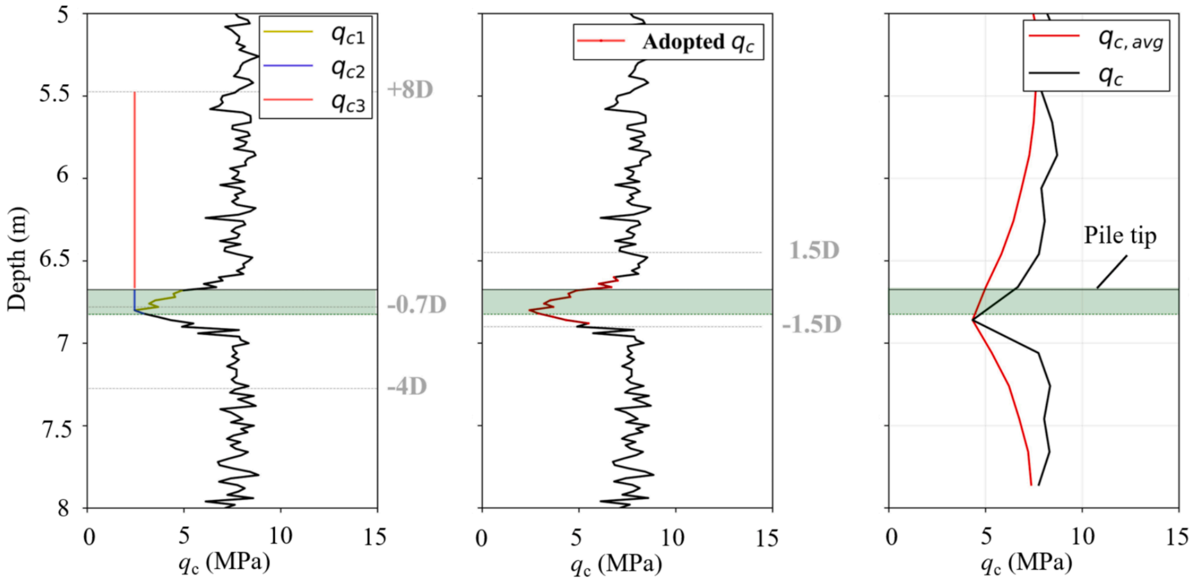

(a) Koppejan method

(b) LCPC method

(c) De Beer method

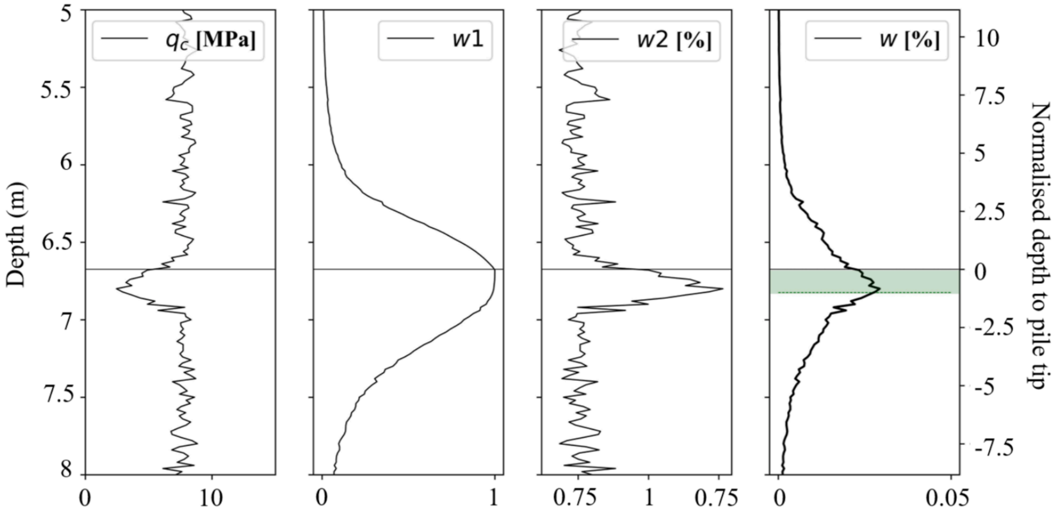

(d) BD-18 method

Fig. 11. Demonstration of averaging methods for a pile in sand with a weak layer at the pile base.

Table 4
Variation of $q_{c,avg}$ determined with different averaging methods.

Soil profile	D (m)	$q_{c,avg}$ (MPa)					
		Koppejan	LCPC	BD-18	De Beer	**Mean**	**CoV**
Sand	0.15	6.67	7.97	7.77	7.20	7.40	7 %
Silt	0.15	1.83	2.10	2.05	1.82	1.95	6 %
L_w = -0.15 m	0.1	3.50	4.52	5.78	4.45	4.56	18 %
	0.15	3.78	5.37	6.25	4.45	4.96	19 %
	PD	8.00 %	18.81 %	8.13 %	0.00 %	8.77 %	–
$L_w = 0$	0.1	2.78	4.47	6.02	4.96	4.56	26 %
	0.15	2.78	4.64	6.47	4.96	4.71	28 %
	PD	0.00 %	3.80 %	7.48 %	0.00 %	3.29 %	–
$L_w = 0.15$ m	0.1	3.17	7.48	6.48	5.56	5.67	28 %
	0.15	3.78	6.97	6.25	4.45	5.36	24 %
	PD	19.24 %	−6.82 %	−3.55 %	−19.96 %	−5.47 %	–

*Note: PD is the percentage difference between results of different pile diameters under the same soil conditions; CoV is the coefficient of variation of $q_{c,avg}$ obtained with the four methods.

most cases) when the weak layer is 0.15 m above or just below the pile tip (L_w = -0.15 and 0 m). The difference is greater (around 19 %) when the weak layer surface is 0.15 m below the pile base (L_w = 0.15 m). This suggests that the Koppejan and the De Beer methods attach relatively high importance to the deep soils below the pile tip in calculating $q_{c,avg}$. In comparison, a significant PD of 18.81 % is observed in the $q_{c,avg}$ values obtained for the two pile diameters with the LCPC method for L_w = -0.15 m, while relatively lower PDs (4 % and 7 %) are observed for other soil profiles (L_w = 0 and 0.15 m). This suggests that, compared to the other three methods, the LCPC method emphasises the soils above the pile tip in calculating $q_{c,avg}$. Specifically, the BD-18 method produces relatively low PDs between 4 % and 8 % for all the weak layer positions.

3.3.3. Variation of the correction factor α_b

Due to the empirical nature of the direct CPT-based design methods, the value of α_b is generally recommended with reference to a specified q_c averaging approach. Therefore, the ability of a q_c averaging approach to generate $q_{c,avg}$ values that yield consistent α_b values across different soil layering and pile sizes is more important than the absolute magnitude of the produced α_b values. This subsection is devoted to examining the variation of α_b values produced by the four averaging methods, thus determining which method is most suitable for use in layered soil conditions. When calculating α_b, the value of $q_{c,avg}$ is taken from Table 4 and the value of $Q_{b\_0.1D}$ or Q_{b_1D} can be drawn from Fig. 8 and Fig. 9, respectively.

Table 5 compares the values of α_b determined for piles in the homogeneous samples. The results show that, under the same failure criteria (0.1*D* or 1*D*), the four methods give similar α_b values. For the 0.1*D* criterion, α_b is around 0.3 for the sand sample and 0.19 for the silt. The lower α_b values for the silt at s/D = 0.1 can be explained by the triaxial responses presented in Fig. 2, where the peak strength was attained after a much greater strain (5 ~ 10 %) in the silt than in the sand (3 ~ 4 %). Under the 1*D* criterion, for both the sand and the silt, α_b is close to 1.0, which means that the pile base capacity Q_{b_1D} is almost equal to the cone tip resistance q_c regardless of soil type. The CoVs in the α_b values obtained with the four methods under both criteria are less than 0.1, indicating consistently comparable performances of the four methods in homogeneous soils.

Figs. 12 and 13 present the α_b values obtained with the four q_c averaging approaches in the layered samples for $Q_{b\_0.1D}$ and Q_{b_1D}, respectively. Fig. 12 shows that when the weak layer is above the pile tip (L_w = -0.15 m), higher α_b values are predicted compared to the other two soil conditions (Fig. 12(b) and 12(c)). This suggests that, if an average α_b is regressively obtained from pile load tests conducted in various soil conditions, this average value tends to underestimate the $Q_{b\_0.1D}$ for L_w = -0.15 m, especially when using the Koppejan and the De Beer methods where the α_b values for L_w = -0.15 m are 2 ~ 3 times those for L_w = 0. Furthermore, a notable scale effect is observed for this soil condition, as indicated by the greater difference in the α_b values compared to other soil layering conditions when using the same averaging method. For instance, the difference in the α_b values between two pile sizes using the Koppejan and the De Beer methods is as great as 0.12 and 0.27, respectively.

Among the four examined q_c averaging approaches, the LCPC method produces the least variable α_b in terms of the scale effect, with the difference in α_b between the two pile sizes generally less than 10 %, thus this method is capable of incorporating scale effect into $q_{c,avg}$. When the weak layer is below the pile base (Fig. 12(b) and (c)), the BD-18 methods demonstrate a similar ability to incorporate the scale effect into $q_{c,avg}$, with differences in the produced α_b values between the two pile sizes being only 0.01 or 0.02.

In terms of the ability to account for soil layering changes, the BD-18 method produces the most consistent α_b values across all soil layering conditions, ranging from 0.11 to 0.39. In comparison, the other methods exhibit wider ranges of α_b (0.25 to 0.64 for the Koppejan method, 0.14 to 0.55 for De Beer, and 0.15 to 0.45 for LCPC). Overall, the BD-18 averaging method outperforms the other three methods in predicting $Q_{b\_0.1D}$ for piles of different sizes in layered soils.

Fig. 13 presents the α_b values calculated from the simulated Q_{b_1D} and the $q_{c,avg}$ values obtained with the four averaging approaches. A comparison with Fig. 12 reveals that the variation of α_b with soil profiles is more pronounced for Q_{b_1D} than for $Q_{b\_0.1D}$. However, among the three soil profiles considered, the highest α_b still occurs when the weak layer is above the pile tip (L_w = -0.15 m). Additionally, for this soil profile, all four methods produce α_b greater than 1, as shown in Fig. 13(a), suggesting that the weakening effect of the silt layer just above the tip is overestimated in the four averaging methods, with the BD-18 method resulting in the lowest overestimation. On the other hand, the ability of the averaging methods to account for the scale effect in $q_{c,avg}$ decreases when analysing Q_{b_1D} compared to $Q_{b\_0.1D}$. Specifically, when the weak layer is situated just below the pile tip (Fig. 13(b)), the maximum differences in the α_b values for different pile sizes range from 0.24 (the BD-18 method) to 0.63 (the Koppejan method), corresponding to relative differences of about 40 % for the BD-18 method and about 60 % for the De Beer method. In contrast, the corresponding differences in the α_b values for $Q_{b\_0.1D}$ (Fig. 12(b)) are much smaller in both absolute and relative magnitudes. Among the four q_c averaging approaches examined, the BD-18 method demonstrates the best performance in producing less variable α_b values across different soil profiles and pile diameters.

Table 5
Correction factor α_b corresponding to the $q_{c,avg}$ values determined using different q_c averaging methods for homogeneous soil samples.

Soil profile	Settlement	α_b					
		Koppejan	LCPC	BD-18	De Beer	Mean	CoV
Sand	0.1*D*	0.33	0.28	0.29	0.31	0.3	0.073
	1*D*	1.19	1	1.02	1.1	1.08	0.08
Silt	0.1*D*	0.2	0.18	0.18	0.2	0.19	0.061
	1*D*	1.16	1.01	1.04	1.17	1.1	0.075

4. Microscopic results and analysis

Two key issues associated with applying direct CPT-based design methods for piles are mentioned in the abstract: the scale effect on α_b and the selection of q_c averaging approaches. The foregoing analysis indicates that these issues disappear in homogeneous soil conditions, suggesting that the soil layering effect is the underlying cause. Therefore, the following microscopic analysis will focus on how soil layering affects the contributions of different layers to pile base resistance (relating to q_c averaging methods) and the strength mobilisation levels in soils surrounding the pile (relating to α_b). Results from the CPT simulations and Tests 1, 3, 4 and 5 for the larger pile with D = 0.15 m are selected for the analysis while the tests for the smaller pile with D = 0.1 m are omitted for simplicity.

4.1. Force chains

4.1.1. CPT penetration through the weak layer

Fig. 14 presents the force chains developed around the cone at various locations relative to the weak layer. The response for the simulation in the homogenous sand sample has been presented in Fig. 14 (a) for comparison. In these figures, force chains are represented by cylinders whose radius and colour indicate the magnitude of force in the chain (contact).

In all cases presented in Fig. 14, force chains originated from the cone and extended to the surrounding soils, with the force magnitude decreasing with increasing distance from the cone. In the absence of weak layers, more force chains developed in soils below the cone level, although considerable chains can be observed above the cone level, as shown in Fig. 14(a). This response represents the situation when the

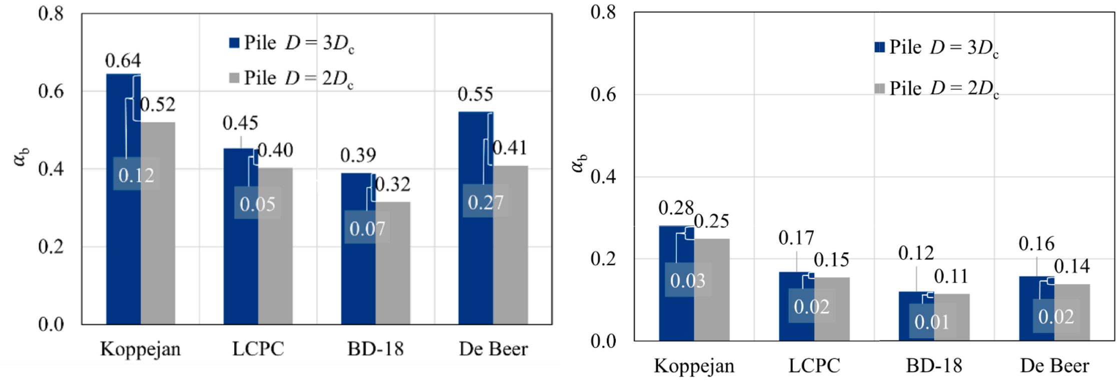

(a) L_w = -0.15 m   (b) L_w = 0

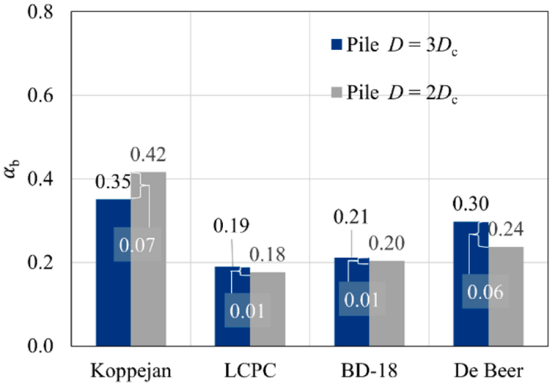

(c) L_w = 0.15 m

Fig. 12. Correction factor α_b for $Q_{b\_0.1D}$ determined by the averaging methods in layered soils.

cone was sufficiently far from the weak layer. When the cone reached a position 0.15 m (~$3D_c$) above the weak silt layer, as shown in Fig. 14(b), the number, length and magnitude of the force chains all decreased compared to Fig. 14(a), with the upper surface of the weak layer significantly hindered the development of force chains into the weak layer and below. Additionally, it is interesting to note that the weak layer, located approximately $3D_c$ below the cone level, also suppressed the development of force chains in soils above the cone level.

As the cone reached the upper surface of the weak layer (Fig. 14(c)), the force chains below the cone level were further weakened, and the force chains above the cone level were in a comparable number to those below the cone level. Meanwhile, some force chains transmitting large contact forces (red cylinders) were formed around the sleeve (the section of the shaft coloured in yellow), which are not seen in Fig. 14(a) and 14(b). This suggests that when the weak layer is located just below the cone level, soils surrounding the sleeve of the penetrometer exhibit increased resistance to penetration, indicating a deformation mode different to that in the homogeneous sand sample. However, this part of the contribution is not reflected in the cone resistance.

In Fig. 14(d), the force chains developed around the cone are much sparser and thinner than those observed in Fig. 14(a). This is also reflected in the q_c profile presented in Fig. 3(c), where the q_c value recorded at the position corresponding to Fig. 14(d) is about half that in the homogeneous sample. However, Fig. 7(b) shows that when the weak layer is just above the pile base (Tests 3 and 6), the values of $Q_{b\_0.1D}$ and Q_{b_1D} are only mildly reduced compared to the homogeneous sample (Test 1). This difference is partly attributed to the size effect, i.e., the relative thickness of the weak layer to the cone diameter is much greater than its relative size to the pile diameters. Besides, CPT installation leads to layer penetration into the underlying layer, as indicated with dashed white lines in Fig. 15. This effect results in a delayed increase or decrease of q_c, depending on whether the underlying layer is stronger or weaker, respectively. This effect does not occur for the bored piles considered in this study, leading to contrasting cone tip and pile base resistances at the same level.

4.1.2. *Influence of the weak layer on the force chain distribution*

Fig. 16 illustrates the force chain distribution surrounding the 0.15 m-diameter pile in Tests 1, 3, 4 and 5, where the location of the weak layer is indicated with two dashed straight lines. Overall, in the simulations involving a weak layer, there is a considerable increase in horizontal force chains within the weak layer. The weak layer significantly impedes stress transmission, forming distinctly different force chain distributions on either side of the interface.

In Test 1 (Fig. 16(a)), where no weak layer is present, robust force chains originate from the pile base and propagate into soils beneath it. Compared to Fig. 14(a), the penetration of the flat-ended pile results in a reduced number of force chains in the shoulders of the pile. This difference is partly due to the increased stresses surrounding the cone as a result of its continuous penetration. Additionally, in a recent DEM simulation of CPTs involving cone penetrometers with varying apex angles, Hunt et al. (2023) revealed that particles below the tip of blunt cones, such as a pile, display more vertical displacement, while sharp-tipped cones induce more horizontal displacements in the surrounding soils. This directional displacement effect causes the force chains beneath a flat-ended pile to propagate primarily in the vertical direction, resulting in a greater concentration of chains propagating into deeper soils rather than the upper soils. This difference between CPT and pile suggests that bored piles at $s/D = 0.1$ have a reduced ability to 'sense' soils above the tip compared to a cone penetrometer. In the context of the BD-18 method (Boulanger and Dejong 2018), this tip shape effect can be addressed by applying a different weighting function to predict $q_{c,avg}$ from $q_{c:true}$ than the one used to derive $q_{c:true}$ from the measured q_c in inverse filtering. Besides, this also suggests that different q_c averaging

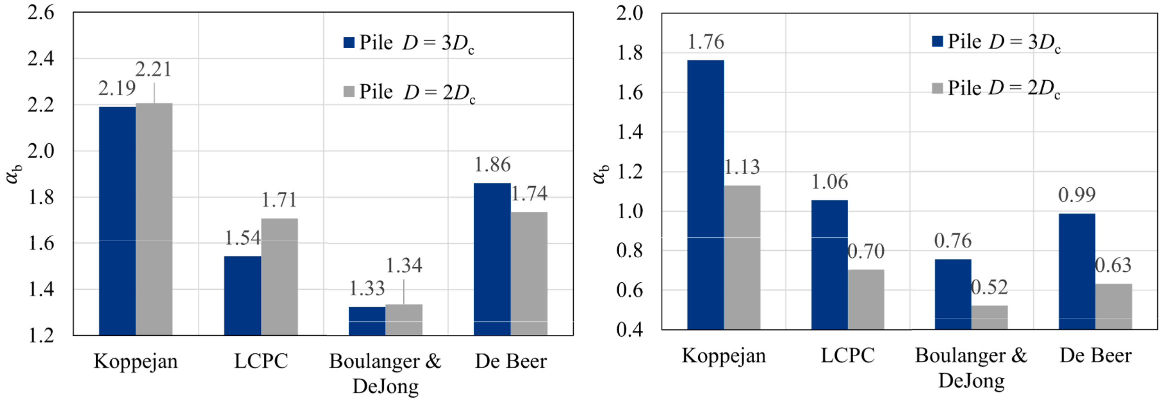

(a) L_w = -0.15 m (b) L_w = 0

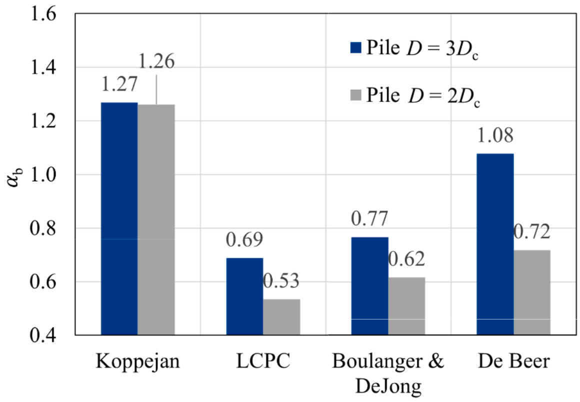

(c) L_w = 0.15 m

Fig. 13. Correction factor α_b for Q_{b_1D} determined by the averaging methods in layered soils.

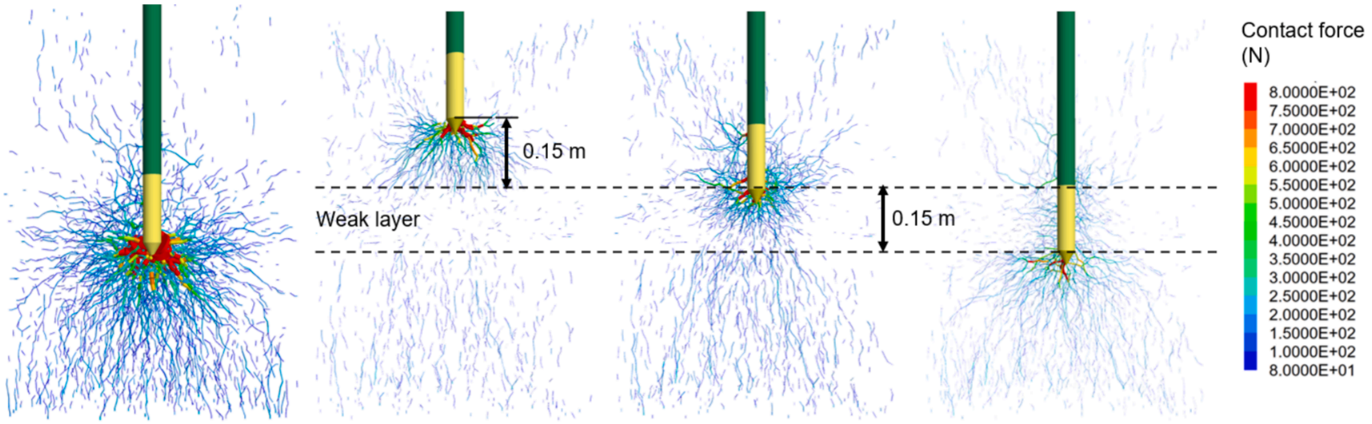

(a) No weak layer (b) L_w = 0.15 m (c) L_w = 0 (d) L_w = -0.15 m

Fig. 14. Force chain development around the cone at various locations relative to the weak layer during the penetration.

methods / weighting functions should be used for bored and displacement piles.

Additionally, Fig. 16 suggests that the high stresses generated below the pile tip cannot be directly transmitted to the shoulders of the pile. Instead, the stresses diffuse to the shoulders through soils outside the region enclosed by the dotted lines indicated in Fig. 16(a), leaving the enclosed zone having much fewer force chains compared to the surrounding areas. The boundary of this zone approximates a logarithmic spiral, resembling the rupture surface for deep foundation proposed by Meyerhof (1951). This resemblance further reveals the zone's formation as a result of stress diffusion affected by directional particle displacements. As will be discussed later, this zone is associated with reduced radial stress. In Test 1, the thickness and height of this zone are about 0.75*D* and 2*D*, respectively.

In Tests 3 and 4, where a weak layer is situated directly above or beneath the pile base (Fig. 16(c) and 16(d)), the zone with reduced force chains disappears or becomes inconspicuous, because of the interruption of stress diffusion by the weak layer. However, when the weak layer is 1*D* below the pile base, as shown in Fig. 16(e), the zone with reduced force chains expands in size as compared to Test 1. In this case, the

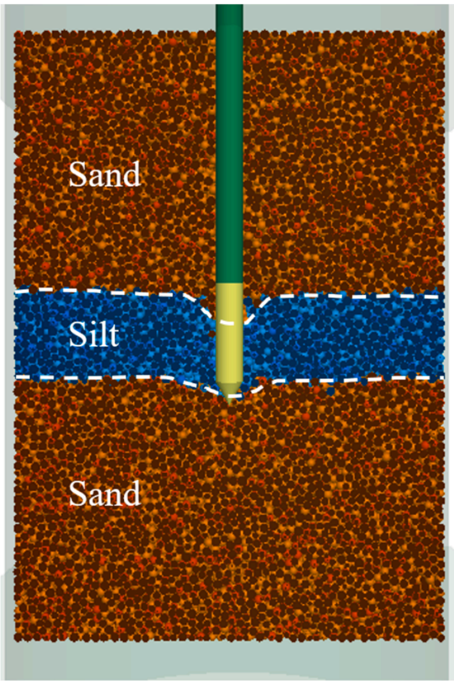

Fig. 15. Weak layer penetration into the sand layer during CPT drilling.

underlying weak layer induces a deformation pattern akin to the punching shear failure mechanism, as indicated by the displacement distribution at 0.5D below the pile base shown in Fig. 17. Here, the vertical settlement within $r/D = 0.5$ in Test 5 is very close to the pile displacement of 0.1D (15 mm) while the radial displacement remains small. This suggests that particle displacement is predominantly vertical in a greater range below the pile tip in Test 5, leading to more directional propagation of force chains and ultimately resulting in a larger zone having reduced force chains.

It is noted that the region with reduced force chains at the shoulder was not observed for the cone penetrometer in Fig. 14. The disparity between the force chain distributions in Figs. 14 and 16(a) arises partly because of the effect of partial mobilisation since the state of $s/D = 0.1$ was considered above. For the state of $s/D = 1$ in Test 1, as shown in Fig. 16(b), the development of force chains into upper soils is more evident compared to Fig. 16(a), and the similarity between the contact force regimes surrounding the tip was restored. This observation suggests that the contribution of different layers to the pile base resistance changes with s/D, i.e. different averaging methods or different weighting functions should be used to obtain $q_{c,avg}$ for different levels of s/D. This characteristic has not been acknowledged in the existing q_c averaging approaches mentioned above.

4.2. *Stress distribution within the soil*

4.2.1. *Stress paths*

Investigating the stress field surrounding the pile can effectively assist in understanding the stress disturbance induced by pile installation and the effect of weak layers. In the following analysis, the stresses surrounding the pile were obtained using measurement spheres with a diameter of 6 times d_{50}, which was found large enough to derive representative stress values. Fig. 18 shows the stress paths followed by soils at different positions around the pile in Test 1. The stress paths obtained from other simulations are similar and hence are omitted for simplicity. The initial states of the soils, indicated with circles in the figure, all exhibit stresses smaller than the in-situ stresses ($p = 66.6$ kPa, $q = 50$ kPa) applied before installing the pile. This suggests that the pile installation resulted in stress decreases in soils, with more decreases induced adjacent to the pile shaft (Points C and D) than below the pile base (Points A and B), as shown in Fig. 18(b).

During the pile loading to $s/D = 0.3$, the stress state of most soils below the pile base rises above the critical state line (CSL) and shifts to greater stresses, as shown in Fig. 18(a). Such stress paths indicate that the soils below the base experienced intense shearing and compression. However, for the pile with the weak layer just below the tip (Test 4, $L_w = 0$), point B was in the silt layer and it follows a stress path approximately parallel to but below the corresponding CSL throughout the simulation (The results are not shown for simplicity). This suggests that the zone experiencing intense shearing and compression is smaller in the silt layer than in the sand. For soils along the shaft, such as Points C and D, the stresses decrease with the increase in s/D and the soils remain below the CSL at $s/D = 0.3$. The stress path behaviours discussed above are in good agreement with those observed around a cone penetrometer or displacement pile in existing DEM simulations (Zhang and Wang 2015; Guo et al. 2024).

4.2.2. *Radial stress distribution*

In calibration chamber tests, it has been found that the pile base resistance or CPT q_c depends primarily on the horizontal stress but is relatively insensitive to the vertical stress (Houlsby and Hitchman 1988). Therefore, the analysis of the stress fields developed around the pile will focus exclusively on the radial stress (σ_r) in the following. Fig. 19 presents the values of σ_r measured in different simulations at $s/D = 0.1$ along the pile shaft. The stresses were taken at a radial distance (r) of 0.286D from the pile axis, where the measurement spheres just touched the pile shaft, similar to the positions of measurement spheres C and D shown in Fig. 18. The vertical distance to the pile base, $h = z - z_{tip}$, is positive for upper soils, and vice versa. As shown in Fig. 19(a), the variation trend of σ_r in different simulations is similar: σ_r is small at positive h/D values, increases with depth to a peak at $h/D \approx -0.5$, and then decreases to the in-situ radial stress at larger depths.

Fig. 19(a) suggests that the peak σ_r in soils beneath the pile base is related to the magnitude of $Q_{b\_0.1D}$. Tests 1 and 3 exhibit the greatest and similar peak σ_r, followed by Tests 5 and 4, which are in the same sequence of $Q_{b\_0.1D}$ in the simulations, as shown in Fig. 7. Additionally, with the increase of depth, σ_r quickly drops to the in-situ radial stress at $h/D = -1.7$ in Test 4 (L_w = -0.15), followed by Test 5 ($L_w = 0.15$) at $h/D = -2.6$. In contrast, the σ_r in Tests 1 and 3 remains slightly above the in-situ stress at $h/D = -3.4$. This suggests that the existence of a weak layer beneath the pile base reduces the zone of influence, with the reduction being more significant when the weak layer is closer to the pile base. Additionally, Fig. 19(a) also shows that the underlying weak layer has a small influence on the stress distribution above the pile base, with σ_r in soils above the pile base being smaller than the in-situ stress. This response is associated with the zone with reduced force chains identified in Fig. 16(a) and 16(e). However, when the weak layer is above the pile tip (Test 3), σ_r is greater than the in-situ radial stress up to $h/D = 1.1$, i.e., the increased radial stresses occurred within the weak layer. The radial stress in the silt layer increased due to the lower friction angle of this material (Table 2), which led to a higher K_0 value.

In existing laboratory and DEM studies on CPT or displacement pile installation in siliceous sand (Jardine et al. 2013b; Yang et al. 2014; Guo et al. 2024), it has been observed that the normalised radial stress (σ_r/q_c or σ_r/Q_b) in soils below the tip level initially increases and attains a peak value when the penetrometer tip reaches the depth of the soil (i.e. $h \approx 0$). This peak value decreases with increasing radial distance (r) from the penetrometer but appears relatively insensitive to the relative density of the sand. Due to these characteristics, the ratio σ_r/Q_b can be considered an indicator of strength mobilisation levels in soils.

In Fig. 19(b), the σ_r values presented in Fig. 19(a) are normalised by the corresponding Q_b (i.e. $Q_{b\_0.1D}$). The results show that the level of strength mobilisation, as reflected by σ_r/Q_b, is primarily controlled by soil type. In Tests 1, 3 and 5, the peak σ_r/Q_b all occurred in the sand layer, and the values are similar and lower than those in Test 4, where

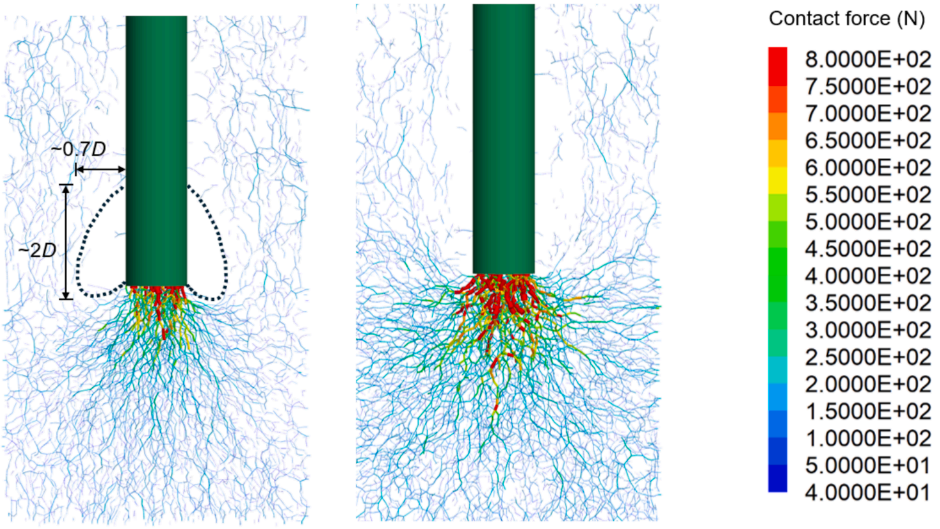

(a) Test 1, s/D = 0.1

(b) Test 1, s/D = 1

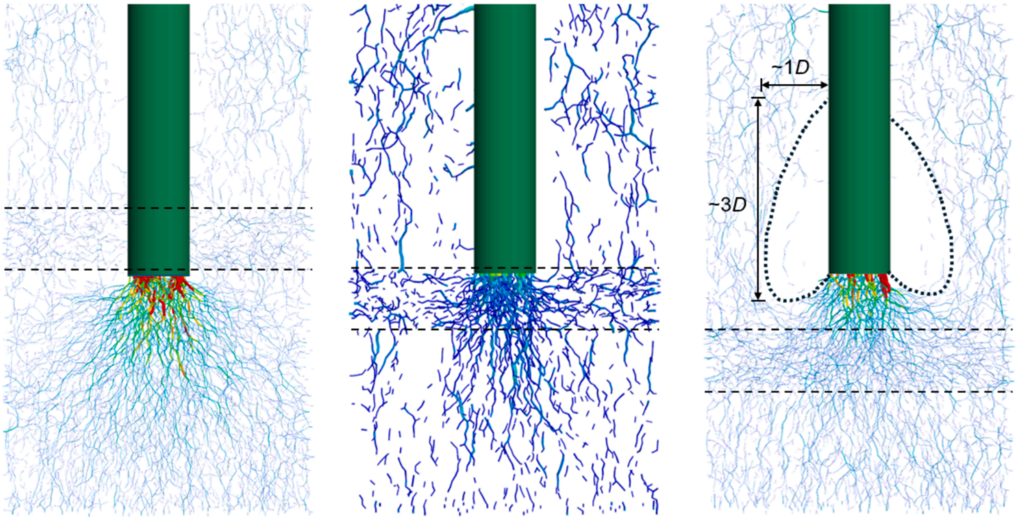

(c) Test 3, s/D = 0.1

(d) Test 4, s/D = 0.1

(e) Test 5, s/D = 0.1

Fig. 16. Force chain development around the pile at $s/D = 0.1$ in the simulations with varying weak layer positions.

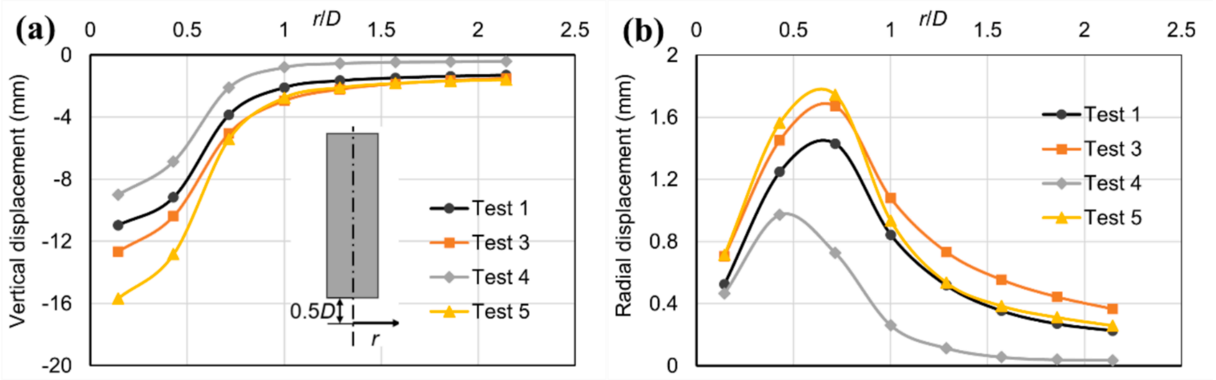

Fig. 17. The distribution of (a) vertical displacement and (b) radial displacement of particles along the radial direction at 0.5D below the pile base in different tests.

the pile base is in the weak silt layer. Notably, the peak σ_r/Q_b of 24.8 % in Test 4 is comparable to the peak σ_r/q_c values of 18.4 to 24.8 % reported by Jardine et al. (2013) in calibration chamber CPTs at $r/D = 1$. The greater σ_r/Q_b value in the weak layer than in the sand is consistent with Lehane et al.'s (2022) observation that the mobilisation of steady-state tip resistance in loose sand requires less penetrometer displacement than in dense sand. For the same pile displacement (0.1D) to be accommodated by soils beneath the pile, more strains will occur in the

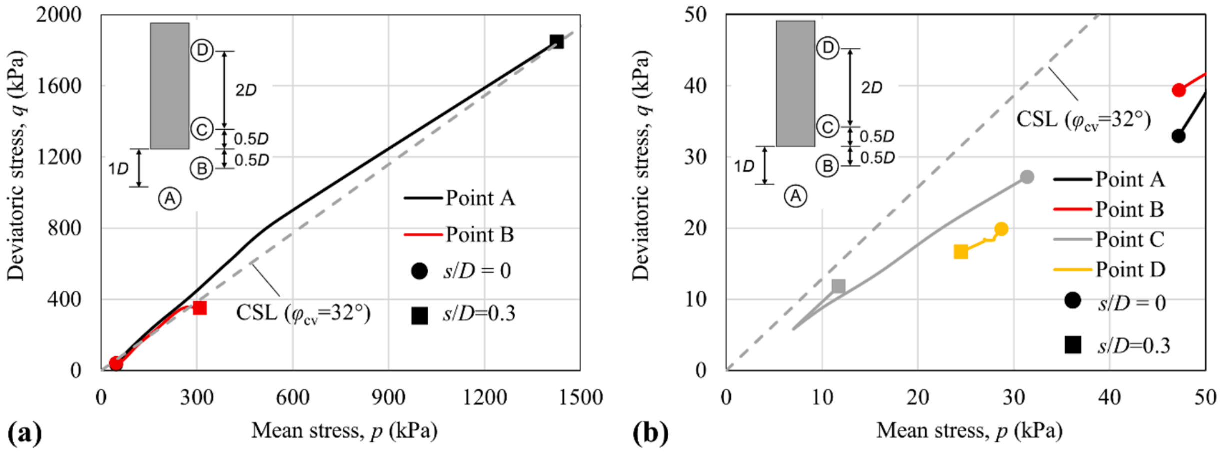

Fig. 18. Stress paths followed by a) soils below the pile base and b) soils along the pile shaft during the loading process in Test 1.

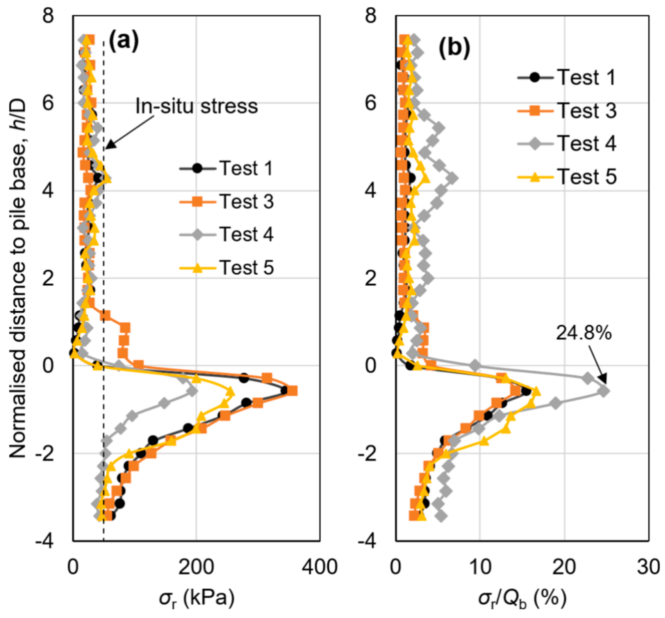

Fig. 19. Variation of radial stress (σ_r) along pile shaft at a normalised radial distance of $r/D = 0.286$ for $s/D = 0.1$.

soils directly below the pile in Test 4, where the zone of influence is the smallest, as inferred earlier from Fig. 19(a).

Further evidence of higher levels of strength mobilisation in the weak layer directly beneath the pile base in Test 4 can be obtained from Fig. 20, which presents the variation of σ_r/Q_b with normalised radial distance (r/D) at different depths (h) beneath the pile base. The figure shows that in all cases, the radial distance (r) at which peak σ_r/Q_b occurred increases with increasing depth, which is a consequence of stress diffusion in soils below foundations. In existing experiments (Jardine et al. 2013b; Yang et al. 2014) and DEM simulations (Guo et al. 2024), the peak σ_r/Q_b directly below the pile base is extrapolated to be about 0.33, corresponding to a fully mobilised state. The peak σ_r/Q_b recorded at $h/D = -0.325$ and $r/D = 0$ in Test 4 (Fig. 20(c)) is similar to this fully mobilised value, suggesting that the soils in Test 4 did reach the highest level of strength mobilisation among the four tests compared. Using σ_r/Q_b as a measure of the strength mobilisation level of soils, it is found that a weak layer directly above the pile tip, such as seen in Test 3, facilitates the strength mobilisation in soils below the pile base, which in turn facilitates the mobilisation of base resistance Q_b.

Additionally, the distribution of σ_r/Q_b in Tests 1 and 5, which involve lower strength mobilisation levels, exhibits peak σ_r/Q_b values at $r > 0$, as shown in Fig. 20(a) and 20(d). In contrast, Fig. 20(b) and 20(c) demonstrate that in Tests 3 and 4, peak σ_r/Q_b values for $h/D > -0.5$ occur at $r = 0$. At low levels of strength mobilisation, the plastic zone originates from the edge of rigid foundations, leading to a saddle-shaped distribution of stresses (Terzaghi et al. 1996) with the peak stress occurring at the edge of the foundation (i.e. $r/D = 0.5$). As the load level increases, the stress peak gradually shifts towards the centre, resulting in an arch-shaped distribution at a fully mobilised state. Consequently, the occurrence of peak σ_r/Q_b vertically below the pile axis ($r = 0$) further reveals that the soils below the pile base in Test 4 exhibit higher strength mobilisation levels.

However, it should be noted that the mobilisation level of base capacity at $s/D = 0.1$ can also be quantified by ratio $Q_{b\_0.1D}/Q_{b\_1D}$. Based on the data from Figs. 8 and 9, this ratio is calculated to be 0.28, 0.29, 0.16, and 0.28 for Tests 1, 3, 4 and 5, respectively. This suggests that the level of strength mobilisation in Test 4 is the lowest among the four tests, which contradicts the implication of σ_r/Q_b. In fact, $Q_{b\_0.1D}/Q_{b\_1D}$ is not suitable for characterising the strength mobilisation level in Test 4, where a 0.15-m weak layer is directly below the pile base; at $s/D = 1$ in Test 4, the pile base sits directly on the underlying sand layer, representing an end-bearing state distinct from that at $s/D = 0.1$.

Except for Test 4, which considers an unrealistic end-bearing state, both σ_r/Q_b and $Q_{b\_0.1D}/Q_{b\_1D}$ indicate that the strength mobilisation levels in the other three tests (Tests 1, 3 and 5) are very similar, supporting the use of a constant α_b value for different soil layering (Lehane et al. 2007).

5. Conclusions

This study utilises parallel DEM simulations of CPTs and pile load tests to investigate the application of direct CPT-based methods for bored piles in layered soils. The numerical model for simulating the pile load tests was constructed using a DEM-FDM coupling technique, where the central region close to the pile was represented as a DEM subdomain comprising discrete particles, while the surrounding region was discretised using continuum meshes solved through FDM. The soil systems under investigation include homogeneous sand and silt samples, as well as layered samples featuring a single silt layer interbedded within the sand at varying depths near the pile base. Two pile diameters were considered in the simulations for studying the scale effect on the correction factor α_b. The macroscopic results were used to examine the suitability of four existing q_c averaging methods for predicting the base capacity of bored piles in layered soils. The stress and force chain distributions in the DEM model were also analysed. The conclusions drawn from this study are as follows:

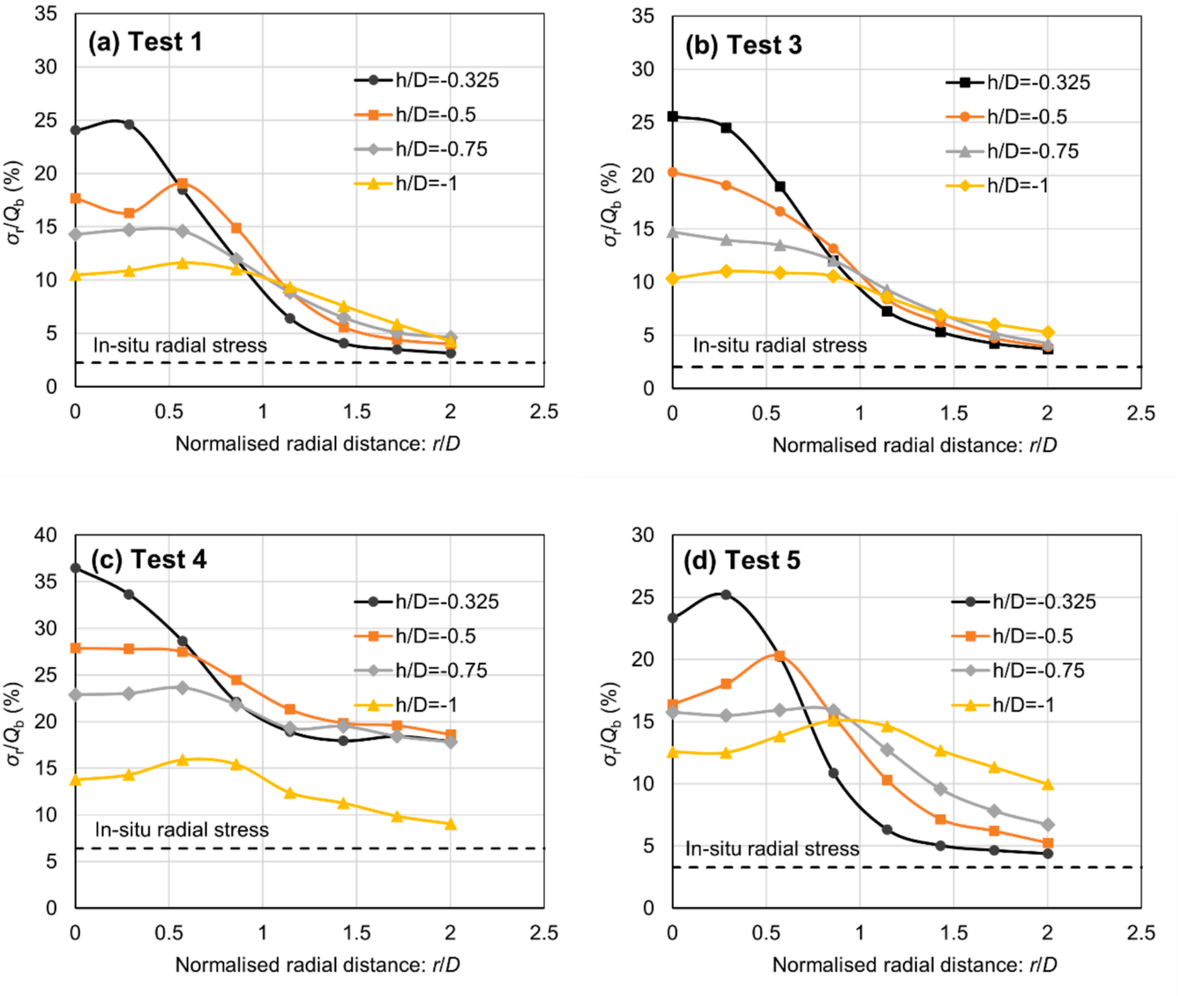

Fig. 20. Variation of radial stress (σ_r) with normalised radial distance (r/D) at different depths beneath the pile for $s/D = 0.1$.

1) The scale effect is influenced by both soil layering and pile displacement. In the initial loading stages (up to 0.3D settlement), the scale effect on pile base resistance is insignificant, unless a soft layer is directly above the pile tip. However, in later loading stages, especially when $s > 0.5D$, the soft layer above the pile base does not induce a significant scale effect on the pile base resistance, while a weak layer closely below the pile tip reduces the pile base resistance, with smaller diameter piles experiencing a more pronounced reduction.
2) The simulated pile and CPT responses were utilised to evaluate the performance of four q_c averaging methods. These methods perform similarly for homogeneous soils, yielding α_b values of 0.3 and 0.19 for pile base resistance ($Q_{b\_0.1D}$) at 0.1D settlement in the homogeneous sand and silt samples, respectively, and of around 1.0 for the ultimate bearing capacity (Q_{b_1D}) in both samples. For layered soils, the LCPC and BD-18 methods effectively account for the scale effect in $q_{c,avg}$, resulting in less variable α_b values for piles of different sizes. The BD-18 method outperforms the others in producing more consistent α_b values across various soil profiles.
3) Soils above the pile tip were found to contribute less to the pile base resistance at $s/D = 0.1$ than to the tip resistance of a cone penetrometer due to the shape discrepancy between their tips. This shape effect suggests that a different weighting function should be used to predict the average cone tip resistance $q_{c,avg}$ for pile from the true resistance $q_{c:true}$ than the one used to derive $q_{c:true}$ from the measured q_c in inverse filtering. However, the similarity between the force chain distributions surrounding the pile and the cone was restored at high levels of s/D, suggesting that the relative contribution of different soil layers to pile base resistance changes with s/D.
4) Except for one simulation that considers an unrealistic end-bearing state of the pile, the strength mobilisation levels in other soil layering conditions are very similar, supporting the use of a constant α_b value for different soil layering.

CRediT authorship contribution statement

Fei Chai: Writing – original draft, Visualization, Methodology, Investigation, Formal analysis, Data curation, Conceptualization. **Bo Liu:** Writing – review & editing, Visualization, Investigation, Formal analysis. **Jianfeng Xue:** Writing – review & editing, Supervision, Project administration, Methodology, Funding acquisition, Conceptualization. **Kevin Duffy:** Writing – review & editing, Methodology, Investigation.

Declaration of competing interest

The authors declare that they have no known competing financial interests or personal relationships that could have appeared to influence the work reported in this paper.

Acknowledgements

The first author received scholarships from UNSW for his PhD research.

Data availability

Data will be made available on request.

References

Al-Baghdadi, T., Davidson, C., Brown, M.J., Knappett, J.A., Brennan, A., Augarde, C., Coombs, W., Wang, L., Richards, D., Blake, A., 2017. CPT-based design procedure for installation torque prediction for screw piles installed in sand. In: Offshore Site Investigation Geotechnics 8th International Conference Proceedings. Society for Underwater Technology, London, pp. 346–353.

Alshibli, K.A., Batiste, S.N., Sture, S., 2003. Strain localization in sand: plane strain versus triaxial compression. J. Geotech. Geoenviron. 129, 483–494. https://doi.org/10.1061/(asce)1090-0241(2003)129:6(483).

Arroyo, M., Butlanska, J., Gens, A., Calvetti, F., Jamiolkowski, M., 2011. Cone penetration tests in a virtual calibration chamber. Géotechnique 61, 525–531. https://doi.org/10.1680/geot.9.P.067.

Arshad, M.I., Tehrani, F.S., Prezzi, M., Salgado, R., 2014. Experimental study of cone penetration in silica sand using digital image correlation. Géotechnique 64, 551–569. https://doi.org/10.1680/geot.13.P.179.

Atkinson, J.H., 2000. Non-linear soil stiffness in routine design. Géotechnique 50, 487–508. https://doi.org/10.1680/geot.2000.50.5.487.

Bagbag, A.A., Lehane, B.M., Doherty, J.P., 2019. Settlement of deep footings in reconstituted sand. Can. Geotech. J. 56, 449–459. https://doi.org/10.1139/cgj-2017-0574.

Bittar, E., Lehane, B.M., Blake, A., Richards, D., White, D., Mahdavi, S., Cerfontaine, B., 2023. CPT-based design method for helical piles in sand. Can. Geotech. J. 61, 102–117. https://doi.org/10.1139/cgj-2022-0209.

Bittar, E.J., Tian, Y., Lehane, B.M., 2022. Application of a new qc averaging approach for end bearing of driven piles in sand. In: Cone Penetration Testing 2022 - Proceedings of the 5th International Symposium on Cone Penetration Testing, CPT 2022. CRC Press, pp. 832–837.

Boorder, M., De Lange, D., Gavin, K., 2022. An alternative CPT averaging procedure to estimate pile base capacity. In: 11th International Conference on Stress Wave Theory and Design and Testing Methods for Deep Foundations. Rotterdam, Netherlands.

Boulanger, R.W., Dejong, J.T., 2018. Inverse filtering procedure to correct cone penetration data for thin-layer and transition effects, in: Cone Penetration Testing 2018 - Proceedings of the 4th International Symposium on Cone Penetration Testing, CPT 2018. CRC Press, pp. 25–44.

British Standards Institution (BSI), 2015. BS 8004:2015 - Code of practice for foundations.

Burland, J.B., 1989. Ninth Laurits Bjerrum Memorial Lecture: "Small is beautiful"—the stiffness of soils at small strains. Can. Geotech. J. 26, 499–516. https://doi.org/10.1139/t89-064.

Bustamante, M., Gianeselli, L., 1982. Pile bearing capacity prediction by means of static penetrometer CPT. In: Proceedings of the 2nd European symposium on penetration testing. Balkema, Amsterdam, the Netherlands, pp. 493–500.

Butlanska, J., Arroyo, M., Gens, A., O'Sullivan, C., 2014. Multi-scale analysis of cone penetration test (CPT) in a virtual calibration chamber. Can. Geotech. J. 51, 51–66. https://doi.org/10.1139/cgj-2012-0476.

Cerfontaine, B., Ciantia, M., Brown, M.J., Sharif, Y.U., 2021. DEM study of particle scale and penetration rate on the installation mechanisms of screw piles in sand. Comput. Geotech. 139, 104380. https://doi.org/10.1016/j.compgeo.2021.104380.

Chow, F.C., 1997. Investigations into displacement pile behaviour for offshore foundations. PhD Thesis, University of London.

Clausen, C.J.F., Aas, P.M., Karlsrud, K., 2005. In: Bearing capacity of driven piles in sand, the NGI approach, in: Frontiers in Offshore Geotechnics. CRC Press, Boca Raton, Florida, pp. 677–681.

Da Cruz, F., Emam, S., Prochnow, M., Roux, J.N., Chevoir, F., 2005. Rheophysics of dense granular materials: Discrete simulation of plane shear flows. PhysRevE 72, 1–17. https://doi.org/10.1103/PhysRevE.72.021309.

De Beer, E., 1971. Methodes de deduction de la capacite portante d'un pieu a partir des resultats des essais de penetration. Ann Trav Publics Belg 1971.

De Cock, F., Legrand, C., Huybrechts, N., 2003. Overview of design methods of axially loaded piles in Europe–Report of ERTC3–Piles. In: IX Deep Foundations Institute International Conference. The Czech Geotechnical Society, Czech Republic, pp. 313–323.

de Kuiter, J., Beringen, F.L., 1979. Pile foundations for large North Sea structures. Mar. Geotechnol. 3, 267–314. https://doi.org/10.1080/10641197909379805.

de Lange, D.A., Terwindt, J., van der Linden, T.I., 2018. CPT in thinly inter-layered soils. In: Cone Penetration Testing 2018 - Proceedings of the 4th International Symposium on Cone Penetration Testing, CPT 2018. CRC press, pp, 383–388.

Duan, N., Cheng, Y.P., Liu, J.W., 2018. DEM analysis of pile installation effect: comparing a bored and a driven pile. Granul. Matter 20, 1–16.

Eslami, A., Fellenius, B.H., 1997. Pile capacity by direct CPT and CPTu methods applied to 102 case histories. Can. Geotech. J. 34, 886–904.

Fellenius, B.H., Harris, D.E., Anderson, D.G., 2004. Static loading test on a 45 m long pipe pile in Sandpoint. Idaho. Can. Geotech. J. 41, 613–628. https://doi.org/10.1139/T04-012.

Ganju, E., Galvis-Castro, A.C., Janabi, F., Prezzi, M., Salgado, R., 2021. Displacements, strains, and shear bands in deep and shallow penetration processes. J. Geotech. Geoenviron. 147, 1–19. https://doi.org/10.1061/(asce)gt.1943-5606.0002631.

Gavin, K., Jardine, R., Karlsrud, K., Lehane, B., 2015. The effects of pile ageing on the shaft capacity of offshore piles in sand. In: In: Frontiers in Offshore Geotechnics III-Proceedings of the 3rd International Symposium on Frontiers in Offshore Geotechnics, pp. 129–151.

Gavin, K., Lehane, B., 2007. Base load – displacement response of piles in sand. Can. Geotech. J. 44, 1053–1063. https://doi.org/10.1139/T07-048.

Geyin, M., Maurer, B.W., 2021. Evaluation of a cone penetration test thin-layer correction procedure in the context of global liquefaction model performance. Eng. Geol. 291, 106221. https://doi.org/10.1016/j.enggeo.2021.106221.

Guo, N., Liu, H.F., Li, B.J., Yang, Z.X., 2024. DEM study of the stress fields around the closed-ended displacement pile driven in sand. Can. Geotech. J. 61, 549–561. https://doi.org/10.1139/cgj-2023-0025.

Han, F., Prezzi, M., Salgado, R., Zaheer, M., 2017. Axial resistance of closed-ended steel-pipe piles driven in multilayered soil. J. Geotech. Geoenviron. 143, 04016102. https://doi.org/10.1061/(asce)gt.1943-5606.0001589.

Houlsby, G.T., Hitchman, R., 1988. Calibration chamber tests of a cone penetrometer in sand. Géotechnique 38, 39–44. https://doi.org/10.1680/geot.1988.38.1.39.

Hunt, O.M., O'Hara, K.B., Chen, Y., Martinez, A., 2023. Numerical and physical modeling of the effect of the cone apex angle on the penetration resistance in coarse-grained soils. Int. J. Geomech. 23, 1–15. https://doi.org/10.1061/(asce)gm.1943-5622.0002626.

Indraratna, B., Ngo, N.T., Rujikiatkamjorn, C., Sloan, S.W., 2015. Coupled discrete element-finite difference method for analysing the load-deformation behaviour of a single stone column in soft soil. Comput. Geotech. 63, 267–278. https://doi.org/10.1016/j.compgeo.2014.10.002.

Issmfe, 1985. Axial pile loading test—Part 1: static loading. Geotech. Test. J. 8, 79–90. https://doi.org/10.1520/GTJ10514J.

Itasca Consulting Group (2021) PFC3D (Particle Flow Code in 3 dimensions) version 7.0.

Iwashita, K., Oda, M., 2000. Micro-deformation mechanism of shear banding process based on modified distinct element method. Powder Technol. 109, 192–205. https://doi.org/10.1016/S0032-5910(99)00236-3.

Jardine, R., Chow, F., Overy, R., Standing, J., 2005. ICP design methods for driven piles in sands and clays. Thomas Telford, London, UK.

Jardine, R.J., Zhu, B.T., Foray, P., Yang, Z.X., 2013a. Measurement of stresses around closed-ended displacement piles in sand. Géotechnique 63, 1–17. https://doi.org/10.1680/geot.9.P.137.

Jardine, R.J., Zhu, B.T., Foray, P., Yang, Z.X., 2013b. Interpretation of stress measurements made around closed-ended displacement piles in sand. Géotechnique 63, 613–627. https://doi.org/10.1680/geot.9.P.138.

Jia, M., Liu, B., Xue, J., Ma, G., 2021. Coupled three-dimensional discrete element–finite difference simulation of dynamic compaction. Acta Geotech. 16, 731–747.

Jia, M., Yang, Y., Liu, B., Wu, S., 2018. PFC/FLAC coupled simulation of dynamic compaction in granular soils. Granul. Matter 20, 76. https://doi.org/10.1007/s10035-018-0841-y.

Jiang, M., Yu, H.S., Harris, D., 2005. A novel discrete model for granular material incorporating rolling resistance. Comput. Geotech. 32, 340–357. https://doi.org/10.1016/j.compgeo.2005.05.001.

Kabeta, W.F., 2022. Effects of full displacement pile installation on the stress and deformation state of surrounding soil. Arch. Civ. Eng. LXVIII 445–466.

Khosravi, A., Martinez, A., Dejong, J.T., 2020. Discrete element model (DEM) simulations of cone penetration test (CPT) measurements and soil classification. Can. Geotech. J. 57, 1369–1387. https://doi.org/10.1139/cgj-2019-0512.

Khosravi, M., DeJong, J.T., Boulanger, R.W., Khosravi, A., Hajialilue-Bonab, M., Sinha, S. K., Wilson, D., 2022. Centrifuge tests of cone-penetration test of layered soil. J. Geotech. Geoenviron. 148, 04022002. https://doi.org/10.1061/(asce)gt.1943-5606.0002716.

Klotz, E.U., Coop, M.R., 2001. An investigation of the effect of soil state on the capacity of driven piles in sands. Géotechnique 51, 733–751.

Lee, J., Salgado, R., 2000. Analysis of calibration chamber plate load tests. Can. Geotech. J. 37, 14–25. https://doi.org/10.1139/t99-061.

Lehane, B., Cosgrove, E., 2000. Applying triaxial compression stiffness data to settlement prediction of shallow foundations on cohesionless soil. Proc. Inst. Civ. Eng. Geotech. Eng. 143, 191–200. https://doi.org/10.1680/geng.2000.143.4.191.

Lehane, B., Liu, Z., Bittar, E., Nadim, F., Lacasse, S., Jardine, R.J., Carotenuto, P., Jeanjean, P., Rattley, M., Gavin, K., 2020. A new 'unified' CPT-based axial pile capacity design method for driven piles in sand. In: in: 4th International Symposium on Frontiers in Offshore Geotechnics. ASCE, pp. 463–477.

Lehane, B.M., 1993. Mechanisms of shaft friction in sand from instrumented pile tests. J. Geotech. Eng. 119, 19–35. https://doi.org/10.1061/(ASCE)0733-9410(1993)119:1(19).

Lehane, B.M., Liu, Z., Bittar, E.J., Nadim, F., Lacasse, S., Bozorgzadeh, N., Jardine, R., Ballard, J.C., Carotenuto, P., Gavin, K., Gilbert, R.B., Bergan-Haavik, J., Jeanjean, P., Morgan, N., 2022a. CPT-based axial capacity design method for driven piles in clay. J. Geotech. Geoenviron. 148, 1–18. https://doi.org/10.1061/(asce)gt.1943-5606.0002847.

Lehane, B.M., Schneider, J.A., Xu, X., 2007. CPT-based design of displacement piles in siliceous sands. Advances in Deep Foundations. CRC Press 81–98.

Lehane, B.M., Zania, V., Chow, S.H., Jensen, M., 2022b. Interpretation of centrifuge CPT data in normally consolidated silica and carbonate sands. Géotechnique 73, 907–916. https://doi.org/10.1680/jgeot.21.00177.

Lopera Perez, J.C., Kwok, C.Y., O'Sullivan, C., Huang, X., Hanley, K.J., 2016. Assessing the quasi-static conditions for shearing in granular media within the critical state soil mechanics framework. Soils Found. 56, 152–159. https://doi.org/10.1016/j.sandf.2016.01.013.

Martinez, A., Frost, J.D., 2016. Particle-scale effects on global axial and torsional interface shear behavior. Int. J. Numer. Anal. Methods Geomech. 41, 400–421. https://doi.org/10.1002/nag.2564.

Mayne, P.W., Dasenbrock, D., 2018. Direct CPT method for 130 footings on sands. In: Zhang, X., Cosentino, P.J., Hussein, M.H. (Eds.), Innovations in Geotechnical Engineering: Honoring Jean-Louis Briaud. Orlando, Florida, pp. 135–146.

McDowell, G.R., Falagush, O., Yu, H.S., 2012. A particle refinement method for simulating DEM of cone penetration testing in granular materials. Géotechnique Letters 2, 141–147. https://doi.org/10.1680/geolett.12.00036.

Meyerhof, G.G., 1951. The ultimate bearing capacity of foundations. Géotechnique 2, 301–332. https://doi.org/10.1680/geot.1951.2.4.301.

NEN 9997-1 (2016) Geotechnical design of structures - Part 1: General rules.

Olson, R.E., Shantz, T.J., 2004. Axial load capacity of piles in Califorlia in cohesionless soils. In: DiMaggio, J.A., Hussein, M.H. (Eds.), Current Practices and Future Trends in Deep Foundations. ASCE, Reston, VA, USA, pp. 1–15.

Pietruszczak, S., Pande, G.N., Oulapour, M., 2003. A hypothesis for mitigation of risk of liquefaction. Géotechnique 53, 833–838. https://doi.org/10.1680/geot.2003.53.9.833.

Poulos, H.G., Davis, E.H., 1980. Pile foundation analysis and design. Wiley.

Robertson, P.K., 2009. Interpretation of cone penetration tests—a unified approach. Can. Geotech. J. 46, 1337–1355.

Sadrekarimi, A., 2016. Evaluation of CPT-based characterization methods for loose to medium-dense sands. Soils Found. 56, 460–472.

Sazzad, M., Biswas, S., Alahy, T., 2014. Determination of relative density of a granularassembly in DEM based modeling, in. In: Proceedings of the 2nd International Conference on Civil Engineering for Sustainable Development, pp. 1286–1290.

Senders, M., Randolph, M.F., 2009. CPT-based method for the installation of suction caissons in sand. J. Geotech. Geoenviron. 135, 14–25. https://doi.org/10.1061/(ASCE)1090-0241(2009)135:1(14).

Su, D., Wu, Z., Lei, G., Zhu, M., 2022. Numerical study on the installation effect of a jacked pile in sands on the pile vertical bearing capacities. Comput. Geotech. 145, 104690.

Su, J., Frost, D., Martşnez, A., 2019. Three-dimensional numerical assessment of axial and torsional interface shear behaviour, in: 7th International Symposium on Deformation Characteristics of Geomaterials. E3S Web of Conferences, pp. 1–6.

Terzaghi, K., Peck, R.B., Mesri, G., 1996. Soil mechanics in engineering practice, Third ed. Wiley.

Van Mierlo, W.C., Koppejan, A.W., 1952. Lengte en draagvermogen van heipalen. Bouw.

Wang, P., Xu, C., Yin, Z.Y., Song, S.X., Xu, C., Dai, S., 2024. A DEM-based generic modeling framework for hydrate-bearing Sediments. Comput. Geotech. 171, 106287.

White, D.J., Bolton, M.D., 2004. Displacement and strain paths during plane-strain model pile installation in sand. Géotechnique 54, 375–397.

White, D.J., Bolton, M.D., 2005. Comparing CPT and pile base resistance in sand. Proc. Inst. Civ. Eng. Geotech. Eng. 158, 3–14. https://doi.org/10.1680/geng.2005.158.1.3.

Xu, X., 2007. Investigation of the end bearing performance of displacement piles in sand. PhD Thesis, University of Western Australia.

Xu, X., Lehane, B.M., 2008. Pile and penetrometer end bearing resistance in two-layered soil profiles. Géotechnique 58, 187–197. https://doi.org/10.1680/geot.2008.58.3.187.

Yang, J., 2006. Influence zone for end bearing of piles in sand. J. Geotech. Geoenviron. 132, 1229–1237. https://doi.org/10.1061/(asce)1090-0241(2006)132:9(1229).

Yang, Z.X., Jardine, R.J., Zhu, B.T., Rimoy, S., 2014. Stresses developed around displacement piles penetration in sand. J. Geotech. Geoenviron. 140, 1–13. https://doi.org/10.1061/(asce)gt.1943-5606.0001022.

Yin, Z.Y., 2022. Three-dimensional numerical modelling of progressive failure of caisson foundation in sand using a coupled FDM–DEM method. Ocean Eng. 253, 111332. https://doi.org/10.1016/j.oceaneng.2022.111332.

Yost, K.M., Green, R.A., Upadhyaya, S., Maurer, B.W., Yerro-Colom, A., Martin, E.R., Cooper, J., 2021. Assessment of the efficacies of correction procedures for multiple thin layer effects on Cone Penetration Tests. Soil Dyn. Earthq. Eng. 144, 106677. https://doi.org/10.1016/j.soildyn.2021.106677.

Zhang, Z., Wang, Y.H., 2015. Three-dimensional DEM simulations of monotonic jacking in sand. Granul. Matter 17, 359–376. https://doi.org/10.1007/s10035-015-0562-4.